Olivine Grain Size Distributions in Faults and Shear Zones: Evidence for Nonsteady State Deformation

Claire Aupart, Kristina G Dunkel, Luiza Angheluta, Hakon Austrheim, Benoit Ildefonse, Anders Malthe-Sørenssen, Bjorn Jamtveit

Olivine Grain Size Distributions in Faults and Shear Zones: Evidence for Nonsteady State Deformation

Claire Aupart[1] , Kristina G. Dunkel[1] , Luiza Angheluta[2] , Håkon Austrheim[1] , Benoit Ildefonse[3] , Anders Malthe-Sørenssen[2] , and Bjørn Jamtveit[1]

[1]Physics of Geological Processes, The Njord Centre, Department of Geosciences, University of Oslo, Oslo, Norway, [2]Physics of Geological Processes, The Njord Centre, Department of Physics, University of Oslo, Oslo, Norway, [3]Géosciences Montpellier, CNRS, University of Montpellier, Université des Antilles, Montpellier, France

Abstract The grain size distribution of deformed rocks may provide valuable information about their deformation history and the associated mechanisms. Here we present a unique set of olivine grain size distributions from ultramafic rocks deformed under a wide range of stress and strain rate conditions. Both experimentally deformed and naturally deformed samples are included. We observe a surprisingly uniform behavior, and most samples show power law grain size distributions. Convincing lognormal distributions across all scales were only observed for samples experimentally deformed at high temperature (1200 °C) and for some mantle-deformed natural samples. Single power law distributions were observed for natural samples deformed by brittle mechanisms and by samples deformed experimentally in the regime of low-temperature plasticity. Most natural samples show a crossover in power law scaling behavior near the median grain size from a steep slope for the larger grain fraction to a more gentle slope for the smaller grains. The small grain fraction shows a good data collapse when normalized to the crossover length scale. The associated power law slope indicates a common grain size controlling process. We propose a model that explains how such a scaling behavior may arise in the dislocation creep regime from the competition between the rate involved in the dislocation dynamics and the imposed strain rate. The common departure from lognormal distributions suggests that naturally deformed samples often have a deformation history that is far from a steady state scenario and probably reflects deformation under highly variable stress and strain rates.

1. Introduction

Localized deformation, brittle or ductile, is normally associated with a significant reduction in the grain size of the rocks involved. In low-temperature cataclastic fault zones, fragmentation takes place by brittle mechanisms and the fragment size distribution often shows a power law size distribution (e.g., An & Sammis, 1994; Billi, 2005; Heilbronner & Keulen, 2006). Grain growth is in most cases only effective at submicron length scales (Sammis & Ben-Zion, 2008).

At higher temperatures grain size reduction may take place by either brittle or ductile mechanisms depending both on the stress level and a range of other factors, including temperature (De Bresser et al., 2001; Stipp et al., 2002), water content (H. Jung & Karato, 2001), crystal orientation (Linckens et al., 2016), strain rate (Stipp et al., 2002), and the presence or absence of multiple phases (Cross et al., 2015; Doherty et al., 1997; Drury & Urai, 1990). The grain size evolution at elevated temperatures is controlled by a competition between grain size-reducing processes and grain growth (e.g., Cross et al., 2015). It is often assumed that the grain size distribution reaches a steady state during dynamic recrystallization (Tasaka et al., 2016), follows lognormal scaling behavior, and is adequately described by its mean value. The mean grain size is often used as a proxy for past stress levels (paleopiezometry; Stipp et al., 2010; Twiss, 1977; Van der Wal et al., 1993). However, as pointed out by Austin and Evans (2007) and Ricard and Bercovici (2009), the grain size reflects the rate of energy dissipation (the scalar product of stress and strain rate) rather than stress alone and is a paleowattmeter rather than a paleopiezometer. This also implies that the entire grain size distribution (rather than the mean value) needs to be taken into account when relating microstructures to mechanisms (Rozel et al., 2011).

Finally, paleopiezometry and paleowattmetry are based on the assumption that the grain size distribution has reached a steady state. This is not a trivial assumption. Numerous studies suggest that the grain size

distribution even in rocks deformed at depth greater than the traditional brittle-ductile transition is often controlled by fragmentation and growth processes that are to some extent separated in time and reflects an initial period of grain size reduction at high stress conditions, followed by recovery and growth at lower stresses (Druiventak et al., 2012; Linckens et al., 2016; Trepmann et al., 2013). Nonsteady state grain size distributions may be more common than hitherto thought and carry valuable information about deformation history beyond the time-independent perspective. In particular, it may contain memory of deformation and growth at very contrasting stress levels.

In this study we present a systematic study of grain size distribution in natural rocks from paleofaults and shear zones and in experimentally sheared rocks. We focus on olivine-rich rocks as representatives of the lithospheric mantle lithologies but include three samples of seismically deformed feldspars and garnets from the lower continental crust for comparison. Our samples, characterized by electron backscattered diffraction (EBSD), show a wide range of grain sizes and microstructures yet a surprisingly consistent grain size scaling behavior. We propose a model for dislocation patterning based on Hähner's (1996a, 1996b) stochastic model to explain the power law behavior observed for the small grain fraction in most of our data set.

2. Acquisition Method

EBSD analyses were made on the CamScan X500FE CrystalProbe at Géosciences Montpellier. Initial processing was made using the CHANNEL5 software suite to remove noise and correct for mineral symmetry. Further processing was done using the MatLab toolbox MTEX (version 4.4.0; http://mtex-toolbox.github.io; Bachmann et al., 2010, 2011; Hielscher & Schaeben, 2008). A misorientation threshold of 10° was applied during grain modeling (a few exceptions are specifically mentioned in the text). Grains smaller than 10 pixels and those with faces on the edges of the orientation map have been excluded for the grain size analysis.

3. Samples

The grain size scaling of deformed rocks will in most cases reflect the influence of both grain fragmentation and grain growth processes. The effects of the growth processes will depend on the relative rates of deformation and growth, and in some situations the growth may have continued long after the fragmentation ceased. We collected data of grain size distributions formed during a wide range of conditions, where the relative influence of fragmentation and growth is different.

Our data can be divided into two subsets. The first one (I) is composed of rocks for which the conditions of deformation are constrained at different levels. These samples come from diverse localities and also include some experimental data. Deformation rates range from seismic faulting to the much slower creep of mantle shear zones. The second set (II) is composed of samples from the Leka Ophiolite Complex (LOC) located in the Central Norwegian Caledonides. This set covers almost the same range of grain sizes as the first set, but the stress and strain rate conditions for the LOC rocks are poorly known. The goal is to use insight gained from the analysis of the first set of data to obtain an increased understanding of the conditions of deformation in a less well understood case, exemplified by the data from the LOC.

3.1. Subset I

3.1.1. Samples From Paleoearthquakes

Paleoearthquakes have been identified through the presence of pseudotachylites, fine-grained rocks believed to have formed during highly energetic events that triggered partial melting of the rocks (e.g., Kirkpatrick & Rowe, 2013; Sibson, 1975). Whereas earthquake slip zones are very narrow, the slip planes are bordered by wider damage zones. In the upper crust this damage zone is usually composed of fault gauge and breccias, often having a power law fragment size distribution (Sammis et al., 1987). However, in the more confined environments at greater depth, fragmentation and recrystallization of wall rocks often seem to take place with very limited shear (e.g., Austrheim et al., 2017; Dunkel, Austrheim, Renard, et al., 2017; Petley-Ragan et al., 2018). We present data on olivine from the Bergen Arcs (Western Norway) and Alpine Corsica ultramafic rocks, as well as on garnet and plagioclase from the Bergen Arcs lower crustal granulites.

One olivine-rich sample (*M02-8a*) comes from a several meters wide lherzolite lens embedded in granulite facies anorthositic rocks and crosscut by pseudotachylite veins on the Holsnøy Island, Bergen Arcs, Norway
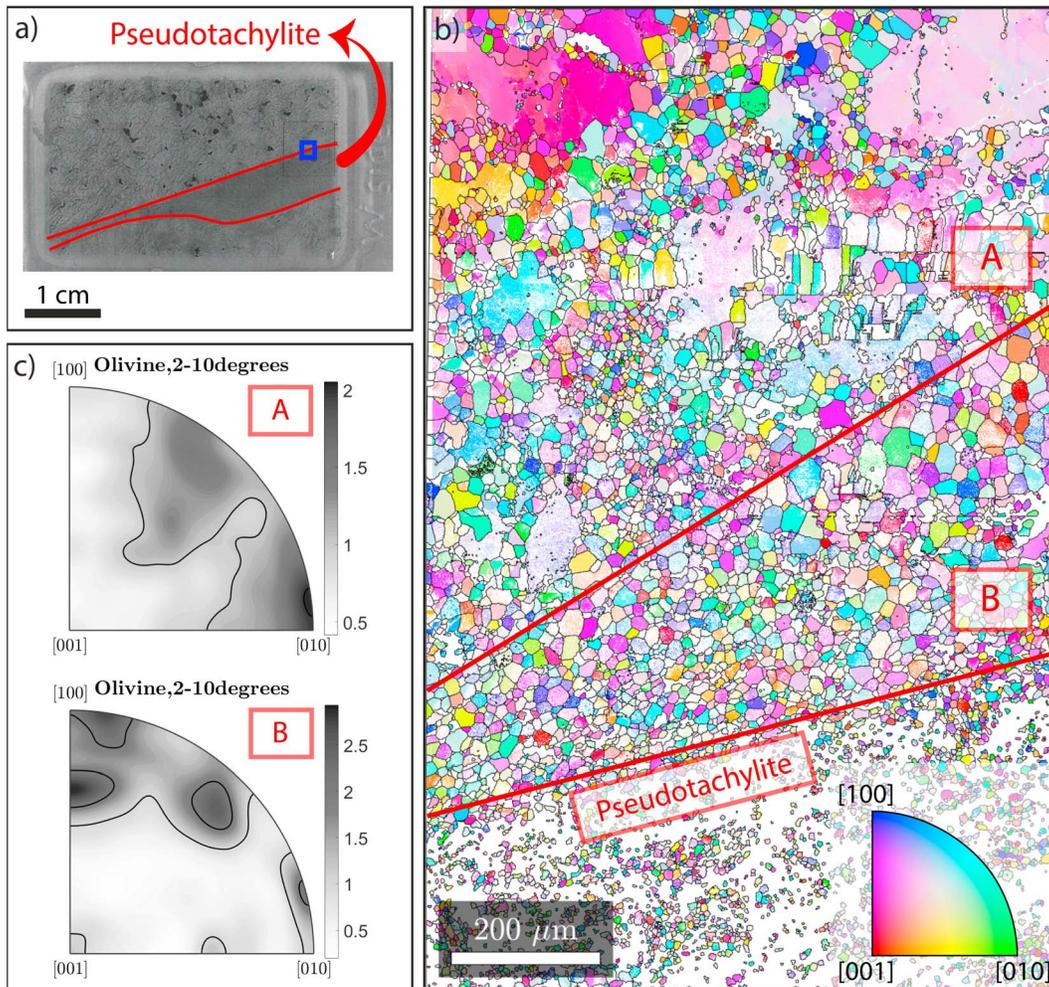
Figure 1. Sample M02-8a. (a) Thin section showing the location of the pseudotachylite in red and the electron backscattered diffraction map (blue square). (b) Olivine orientation map with inverse pole figure color coding. The reference orientation is horizontal. Two zones were defined in the map: Zone B in direct contact with the pseudotachylite and zone A located further from the pseudotachylite and containing olivine porphyroclasts. White areas are clinopyroxenes and orthopyroxenes in the pseudotachylite and mostly orthopyroxenes in zones A and B with some areas of misindexing. These two zones are studied separately and are referred to as M02-8a A and M02-8a B. Horizontal lines drawn by grain boundaries to the left of the zone A label are measurement artifacts. (c) Olivine internal misorientation rotation axes for low angles (2–10°) in zones A and B. Rotation axes are concentrated around [010] in zone A and toward [100] in zone B. Contour lines are drawn for integer multiples of a uniform distribution.

(S. Jung et al., 2014; Kühn et al., 2000). Olivine in this sample is slightly richer in iron than typical mantle olivine (Fo$_{80-85}$). A second olivine-rich sample from Corsica (*Cor19-06*) represents seismically affected peridotites from a high-pressure-low-temperature (blueschist facies) terrain in the Cima de Gratera ophiolitic nappe (Magott et al., 2016). Coseismic slip is indicated by numerous pseudotachylite-filled faults and injection veins. The geological setting was described by Andersen and Austrheim (2006). For each sample, one EBSD map was made of the wall rock adjacent to pseudotachylite containing faults. Two zones can be identified close to the pseudotachylite: Zone A is the outermost area, collected a few hundred micrometers away from the fault, while zone B is located at the immediate contact with the pseudotachylite. In *M02-8a*, one map in each zone has been done (Figure 1). The map done in *Cor19-06* is located inside zone A (Figure 2). In both cases, zone A is porphyroclastic, with misorientation rotation axes (the crystallographic axes around which the crystal lattices of neighboring subgrains are rotated with respect to each other) concentrated around [010]. This suggests that a process similar to slow, crystal-plastic deformation in the mantle was active. Zone B is composed of more polygonal olivine grains with a complex set of misorientation rotation axes, which we interpret as directly related to the pseudotachylite-generating event.

Cor19-06
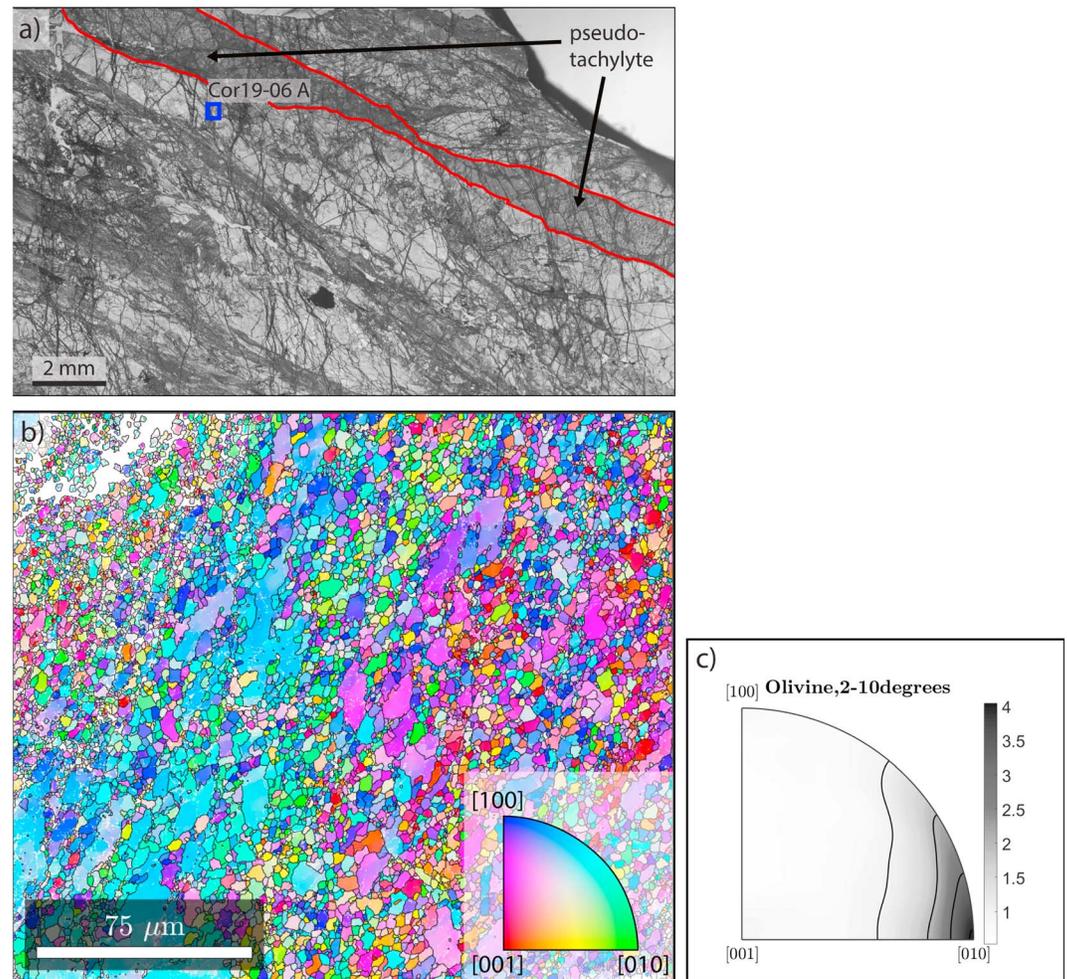
Figure 2. Sample Cor19-06. (a) Image of thin section showing the location of the pseudotachylite in red and the electron backscattered diffraction map (blue square). (b) Olivine orientation map with inverse pole figure color coding. The reference orientation is horizontal. White area in the upper left corner is due to misindexing. The map is located in zone A, that is, not in direct contact with the pseudotachylite and is referred to as Cor19-06 A. The map is rotated 90° clockwise with respect to (a). (c) Olivine internal misorientation rotation axes for low angles (2–10°). Rotation axes are concentrated around [010]. Contour lines are drawn for integer multiples of a uniform distribution.

For comparison with non-olivine silicates, garnet (*ÅF2-4*) and plagioclase (*A16-011 and A16-013A*) samples from wall rocks around pseudotachylite-filled faults through granulite facies anorthosites from Holsnøy, Bergen Arcs, Norway (Austrheim et al., 1996), have also been included. The granulite facies garnets are located within a distance of 2 mm from the pseudotachylite and experienced extensive grain size reduction during earthquakes related to the Caledonian orogeny (Austrheim et al., 2017). Two EBSD maps have been recorded from sample ÅF2-4. Map 1 corresponds to garnet II, and map 2 corresponds to garnet I in Austrheim et al. (2017). Crystal plasticity and possibly also brittle deformation during seismic loading led to an intense fragmentation of the original single crystals, with a smooth transition from subgrains to grains. A 2° threshold has been applied for grain modeling in MTEX to include subgrain data in the analysis. Three EBSD maps were also recorded from fragmented wall rock plagioclase. Two maps (maps 2 and 8) were made from sample A16-011, located approximately 1 mm away from a pseudotachylite, and a third one (map 3) from sample A16-013A, located approximately 10 cm away. These samples are described in more detail by Petley-Ragan et al. (2018; A16-011 map 2 shown in Figure 5a, A16-011 map 8 in Figure 6, and A16-013A map 3 in Figure 7 of the cited reference).

3.1.2. Hydrofractured Samples

To obtain insight into the scaling behavior of a system where growth processes have limited effects on the grain size distribution, we have included a data set that was interpreted to record brittle deformation induced by hydrofracturing (Padrón-Navarta et al., 2010).

Four samples (*Al06-05a*, *-34*, *-35*, and *Al07-07*) from grain size reduction zones in prograde peridotites in the Cerro del Almirez ultramafic massif, Betic Cordillera, Spain, were analyzed. The deformation temperature was estimated to be in the range 680–710 °C. The authors observed features indicating that dislocation creep was not the major deformation process: low dislocation density in grains, few dislocation glide morphologies observed, inherited crystallographic preferred orientation (CPO), high misorientation angles, rotation axis distribution close to random, and remnants of the original crystal shapes. Radial dislocations are indicative of fast fluid assisted growth. More details on the samples are available in Padrón-Navarta et al. (2010).

3.1.3. Samples From *Kick-and-Cook* Experiments

The microstructural effects of deformation at high strain rates (approximately 10^{-4} s^{-1}) followed by an annealing phase at high temperature (between 700 and 1000 °C) were studied in the kick-and-cook experiments of Druiventak et al. (2012) and Trepmann et al. (2013). Their goal was to simulate the effect of recrystallization following coseismic deformation. The samples obtained from these experiments typically show localized grain size reduction zones with a weak CPO independent of the stress field. There are two types of newly formed grains: fragments directly inherited from the porphyroclasts characterized by a high dislocation density, low misorientation angles, and irregular shapes, and recrystallized grains characterized by low dislocation density, nearly random orientation, and concave boundaries (Trepmann et al., 2013).

The samples included in this study (samples *B9006*, *B9010*, *B9014*, *B9028*, *B9029*, *B9036*, and *B9037*) are the products of experiments carried out on natural peridotites from the Almklovdalen peridotite complex in Western Norway. In samples without the annealing step, the authors identify evidences of both brittle and crystal plastic deformation; intragranular microcracks with little offset are the main deformation feature with undulatory extinction concentrated next to shear zones (Druiventak et al., 2011). They observe a larger dispersion of the CPO with increasing annealing temperature (Druiventak et al., 2012; Trepmann et al., 2013). Detailed descriptions of the experimental settings and samples are available in Druiventak et al. (2012) and Trepmann et al. (2013).

An additional sample included here, *Am23b 01*, was described as a natural equivalent to kick-and-cook experimental samples. It is a peridotite from a shear zone in the Balmuccia and Baldissero complexes previously described by Druiventak et al. (2012).

3.1.4. Samples From Torsion Experiments

Paleopiezometry is based on the assumption that the rates of grain size reduction and growth have reached a steady state. The torsion experiments by Tasaka et al. (2016) simulate the effects of steady state shearing without any postdeformational annealing process.

Tasaka et al. (2016) conducted experiments to test the effects of high strain rate torsion (approximately 10^{-4} s^{-1}) on hydrated olivine aggregates at temperatures of 1200 °C. Hydrated conditions were believed to be representative of the lithospheric mantle conditions. Samples were made from a mix of synthetic fayalite power and San Carlos olivine power (Fa_{10}; details on the preparation techniques are given in Zhao et al., 2009). The olivine used during the experiments had a composition near Fo_{50} to facilitate effective deformation since this composition has lower strength compared to natural Fo-rich mantle olivine. The deformed samples show the activity of the [100]{0kl} sliding system expected in mantle rocks plastically deformed at temperatures higher than 1000 °C (e.g., Falus et al., 2011; Hansen et al., 2011; Nicolas & Christensen, 1987; Tommasi et al., 2000). Data from 12 samples (*PT-889*, *PT-892*, *PT-916*, *PT-930*, *PT-933*, *PT-938*, *PT-939*, *PT-952*, *PT-954*, *PT-966*, *PT-973*, and *PT-976*) including two dry (*PT-916* and *PT-930*) and two initial undeformed (*PT-916* and *PT-933*) samples from Tasaka et al. (2016) are presented below.

3.1.5. Mantle-Deformed Samples

All natural and laboratory deformed samples described above, except for the torsion experiment samples, have an initial fabric controlled by plastic deformation in the mantle.

Ten samples (*BC05-101*, *-123*, *NV05-123*, *-128*, *-129*, *-161*, *-162*, *-165*, *-168*, and *-171*) from Falus et al. (2011) consisting of dynamically recrystallized olivine in spinel peridotite xenoliths from Persani Mountains, Southeastern Carpathians, Romania, are included below as representatives of microstructures believed to
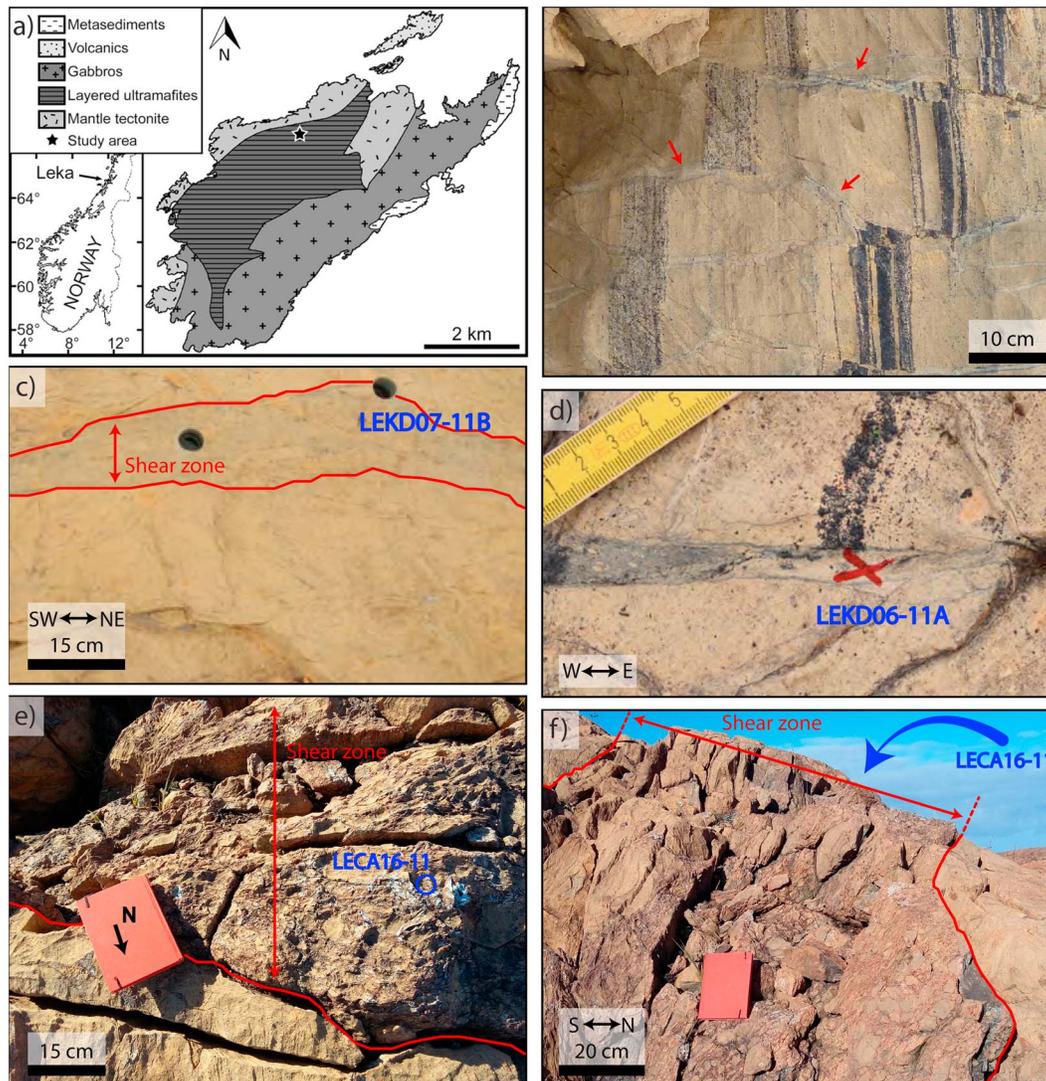
Figure 3. (a) Geological map of the Leka Ophiolite Complex (reprinted from Dunkel, Austrheim, Renard, et al., 2017, with permission from Elsevier), showing the study area of samples from Subset II. (b) Field images showing chromite layers offset by localized faults (red arrows). The fragmented wall rocks of these faults are referred to as zone C by Dunkel, Austrheim, Renard, et al. (2017) and Dunkel, Austrheim, Ildefonse, and Jamtveit (2017). (c) Location of sample LEKD07-11B along a narrow shear zone. (d) Location of sample LEKD06-11A at the tip of a narrow shear zone. (e) Location of sample LECA16-11 in a large shear zone. (f) Side view of the shear zone where LECA16-11 was sampled.

have formed at mantle conditions. Subgrain rotation was the main recrystallization mechanism, and dislocation glide occurred mainly on [100]{0kl} systems.

3.2. Subset II: The LOC

The LOC is part of the Uppermost Allochthon of the Scandinavian Caledonides which has been emplaced during the collision between Laurentia and Baltica during closure of the Iapetus Ocean (Roberts et al., 2007). It is located on the Leka Island around 65°N (Nord-Trøndelag) on the Norwegian west coast and is one of the best exposed and preserved ophiolites in the Scandinavian Caledonides. The LOC has been dated at 497 Ma ± 2 Ma (Dunning & Pedersen, 1988) and comprises a complete ophiolite section (Furnes et al., 1988). Basalts and volcanic rocks have geochemical signatures ranging from mid-ocean ridge basalt to island arc tholeiite, making the LOC a supra-subduction zone-type ophiolite (Furnes et al., 1988). It is situated in a sinistral extensional pull-apart structure, which permitted its preservation (Titus et al., 2002).

Samples from shear zones and faults come from the northwestern part of the island (Figure 3a). The layered ultramafic unit of the LOC consists of alternating layers of harzburgite, dunite, and websterite showing
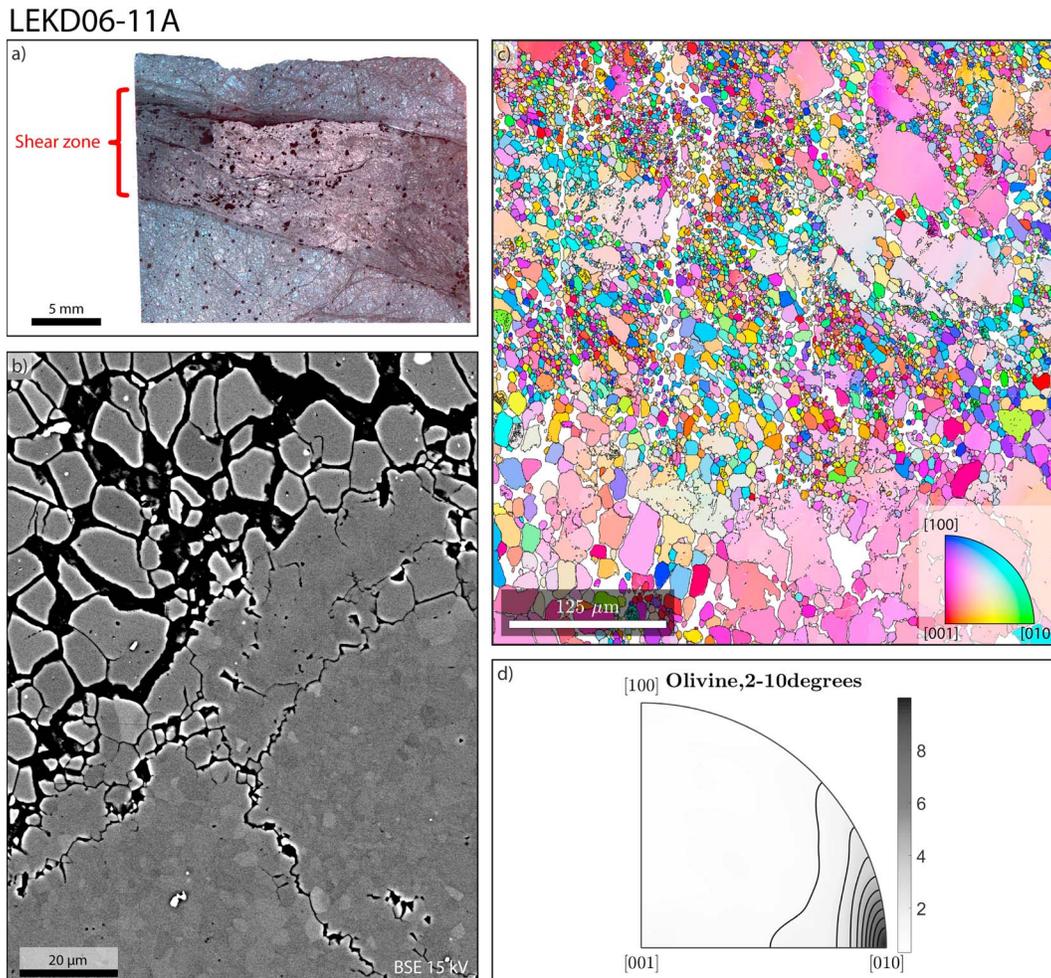
LEKD06-11A

Figure 4. Sample LEKD06-11A. (a) Image of thin section showing the location of the pseudotachylite in red and the electron backscattered diffraction map (blue square). (b) Backscattered electron image showing characteristic microstructures of olivine recrystallization and fragmentation inside the shear band. Bricky olivine is visible near the upper left corner, while subgrains are visible in the lower right corner. The black network is serpentine. (c) Olivine orientation map with inverse pole figure color coding. The reference orientation is horizontal. The white network is serpentine. (d) Olivine internal misorientation rotation axes for low angles (2–10°). Rotation axes are concentrated around [010]. Contour lines are drawn for integer multiples of a uniform distribution.

various degrees of serpentinization. All analyzed rocks are dunites. Faults and shear zones are mostly oriented E-W, vertical, and with offsets ranging from millimeters to tens of meters.

Background (mantle-deformed) samples (*LE04-14 areas 2 and 6*) have been sampled outside the shear zones. They show dynamically recrystallized olivine with dislocation glide on the [100]{0kl} systems (zone A from Dunkel, Austrheim, Ildefonse, & Jamtveit, 2017; Dunkel, Austrheim, Renard, et al., 2017).

Samples *LE05-14 areas 1 and 3* represent damage zones around highly localized faults (Figure 3b) believed to have formed by dehydration embrittlement during dehydration of former serpentine veins (zone C from Dunkel, Austrheim, Ildefonse, & Jamtveit, 2017; Dunkel, Austrheim, Renard, et al., 2017). These samples show brittle fragmentation with very little shear strain, and microstructures predating the deformation can still be identified.

The remaining samples come from shear zones of various widths (Figures 3c–3f). *LEKD06-11A* and *LEKD07-11B* are located close to each other at the tip and the border of approximately 20-cm-wide shear zones, respectively (Figures 3c and 3d). Deformation is restricted to a centimeter-wide shear band with a sharp transition to the host rock in LEKD06-11A (Figure 4a), while it affects most of the thin section in LEKD07-11B with a gradual transition to the host rock. In both samples relatively undeformed olivine with straight boundaries coexist with interlobate grains subdivided into smaller fragments. The microstructures look very similar on

LEKD07-11B
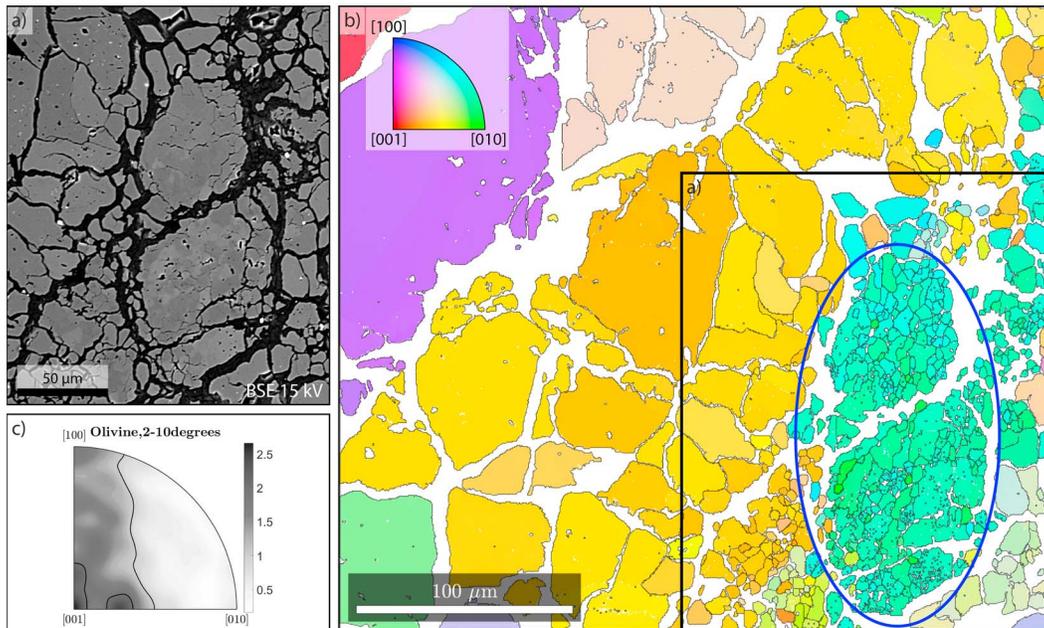
Figure 5. Sample LEKD07-11B. (a) Backscattered electron image of the mapped area. Different shades of gray indicate the presence of subgrains. The black network is serpentine. (b) Olivine orientation map with inverse pole figure color coding. The reference orientation is horizontal. The blue ellipse indicates the area used for grain size distribution analysis. The white network is serpentine. (c) Olivine internal misorientation rotation axes in the blue ellipse for low angles (2–10°). Contour lines are drawn for integer multiples of a uniform distribution.

scanning electron microscopy micrographs (Figure 4b and 5a), but orientation maps show that the grain fragments are subgrains in LEKD07-11B (Figure 5b; a 2° threshold has been used for grain modeling in MTEX), while they are grains in LEKD06-11A (Figure 4c). The low-angle (2–10°) misorientation axes are concentrated around [010] for LEDK06-11A (Figure 4d). In LEKD07-11B, the low-angle misorientation axes are distributed in the plane described by the [100] and [001] axes of the olivine crystals suggesting that the sliding system [010]{h0l} was active during deformation (Figure 5c).

LECA16-11 areas 1 and 2 (Figure 6) come from an approximately 1-m-wide shear zone (Figures 3e and 3f). The two areas display two kinds of domains of newly formed grains (Figures 6a and 6b). The first domain type is composed of rounded to angular domains inside original relatively undeformed grains (such as grains 1 and 2 in Figure 6a). They display angular and often elongated grains, which have undergone little shearing and largely kept the orientation of the host grain (Figures 6a–6d). The second type of domain is composed of equigranular grains with more varied crystal orientations compared to the original crystals (Figures 6a–6d). They are visible in significantly sheared domains between the original relatively undeformed grains. We call the first type fragmented domains and the second type sheared domains. The fragmented domains include both grains and subgrains; thus, grain modeling by MTEX has been done while considering 2° as the minimal misorientation angle between two grains. The misorientation axes distributions for low angles (2–10°) are close to random (Figure 6e). The grains from the two types of domains are identified in the figures as fragments and sheared grains or by the letters f (fragmented) and s (sheared) following the sample number.

4. Grain Size Distributions

In the following, grain size distributions are defined by the probability density functions (pdfs) of the grain cross-section areas. The pdf $f(X) = \frac{dC(x<X)}{dX}$ is related to the cumulative distribution function $C(x < X)$, which includes the grain areas smaller than a given size X. The probability that a grain area is between X and $X + dX$ is given by $f(X)dX$.
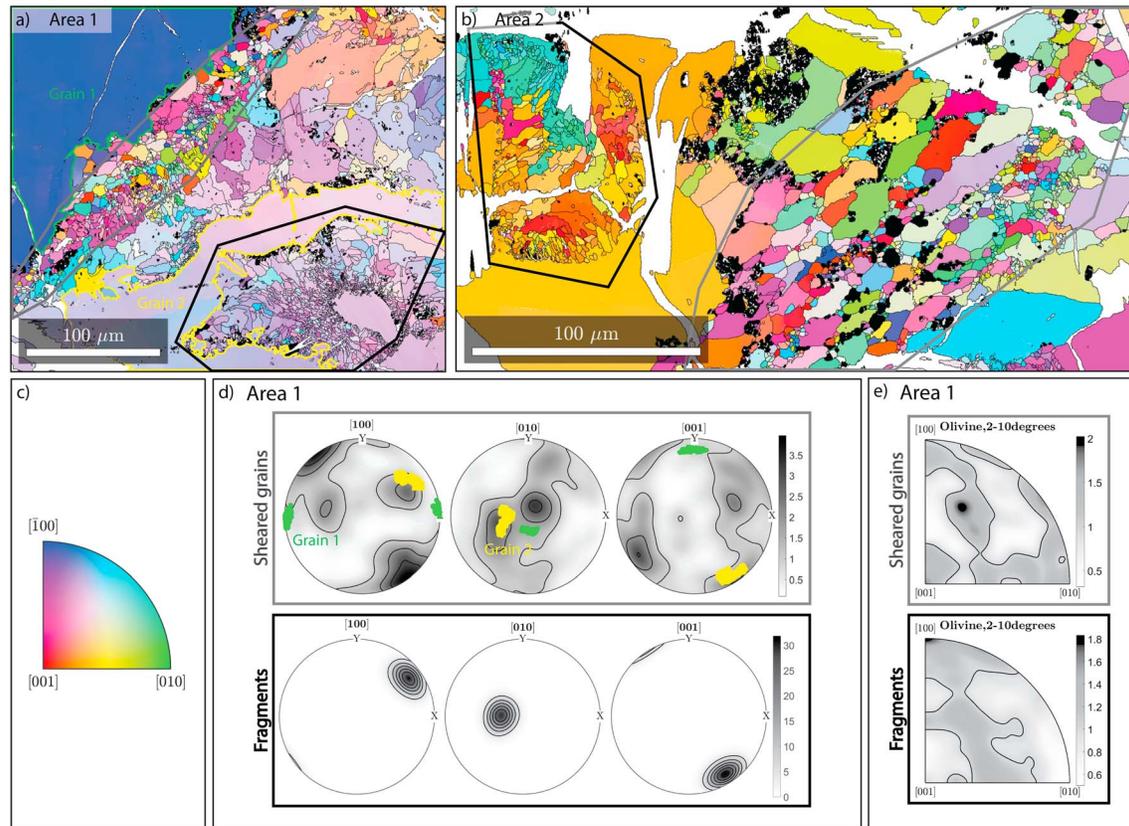
Figure 6. Two electron backscattered diffraction maps were done in sample LECA16-11. (a and b) Olivine orientation map with inverse pole figure color coding of areas 1 and 2, respectively. White areas are serpentine veins and antigorite crystals. Black areas are mostly clinopyroxene grains and a few orthopyroxene and magnetite grains. The domains being used for grain size distributions analysis are marked with black (fragments) and gray (sheared grains) lines. (c) Inverse pole figure color coding for olivine. The reference orientation is horizontal. (d) CPO of the rounded grains and of the fragments. The green and yellow dots in the diagram for sheared grains are the CPO of the two large relatively undeformed grains identified in (a). (e) Olivine internal misorientation rotation axes for low angles (2–10°) for sheared grains and fragments in area 1. Both show almost random rotation axis orientation. Contour lines are drawn for integer multiples of a uniform distribution.

4.1. Curve Fitting

Most attempts to model grain size coarsening or fragmentation have assumed that the entire distribution can be obtained from the mean grain size (Austin & Evans, 2007; De Bresser et al., 2001). This requires that the distributions are self-similar and show similar scaling behavior. It is usually assumed that the distribution is lognormal as suggested by experimental studies of nucleation and growth processes (Feltham, 1957; Kile et al., 2000). However, analyses of our extensive set of data show significant deviations from such a distribution. Samples deformed by brittle processes and by low-temperature plasticity tend to show simple power law scaling behavior reflecting a scale-independent fragmentation mechanism (Figure 7a). Other data sets show a pdf with lower slope for small grains than for large grains. While this is the case for a lognormal distribution (Figure 7b), some of the data sets reveal a much better fit to a combination of two power law segments intersecting at some crossover length than to a continuously curving lognormal function (Figure 7c). A combination of two power laws may arise if two different physical processes operate at different length and time scales. One possibility that will be discussed below is that the steeper distribution of large grains is mainly controlled by fragmentation processes, while the more gentle slopes of the smaller grains are influenced by healing processes operating at shorter length scales.

Fitting laws are described by the parameters given in Figure 7b. For a lognormal distribution, these parameters are μ and σ. The μ is closely linked to the median value of the distribution, and σ is related to the spread of the distribution. The goodness of the lognormal fit is evaluated by the standard error of the regression (S; see the supporting information for the definition of S). S values less than approximately 0.1
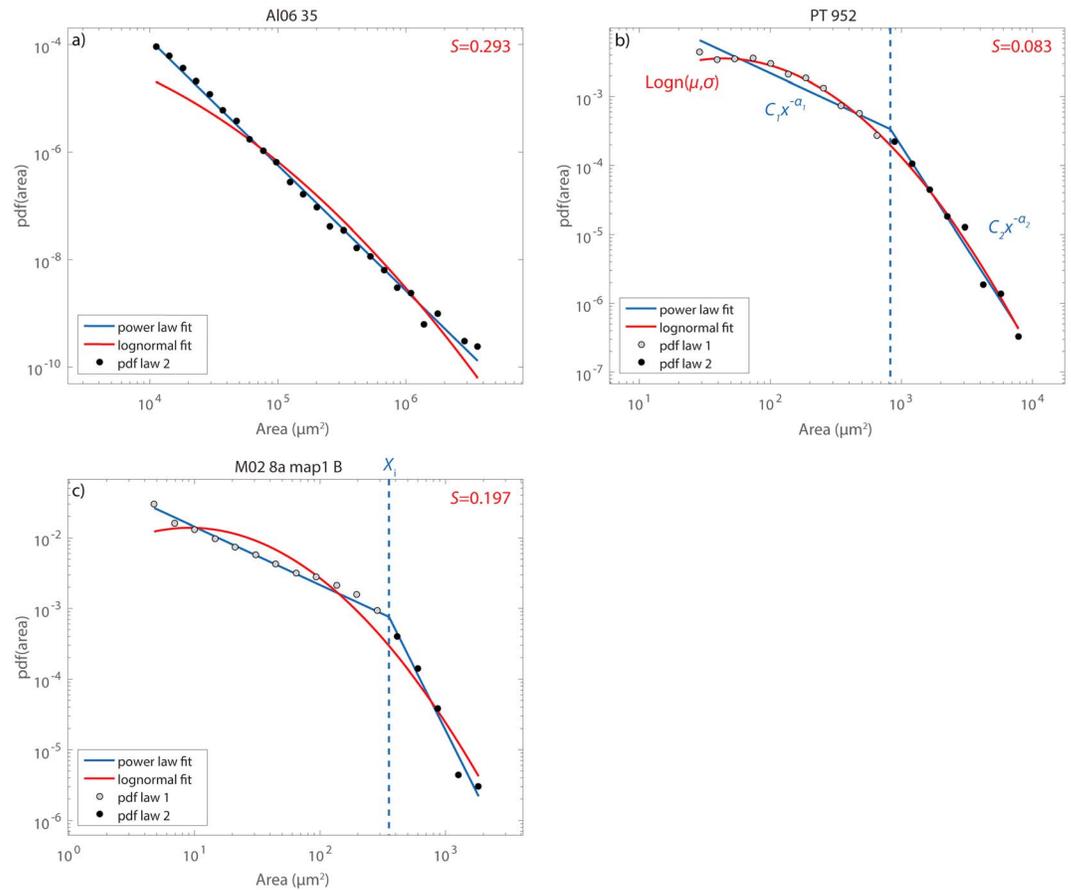
Figure 7. Representative examples of grain size distributions. (a) Probability density function (pdf) of one of the brittle samples from Padrón-Navarta et al. (2010) fitted by both a power law (blue line) and a lognormal law (red line). In this case the simple power law fit is unambiguously the best. (b) pdf of one of the samples deformed by steady state torsion from Tasaka et al. (2016). The distribution is fitted both by a lognormal distribution and two power laws. In this case the fit to a lognormal distribution is best. This figure also shows the parameters describing the lognormal and the power law fits. (c) pdf of one of the samples from the damaged wall rock adjacent to a pseudotachylite. It has been fitted both by a lognormal distribution and a combination of two power laws. In this case the two power laws fit is clearly the best.

are taken to indicate a good fit to a lognormal distribution (e.g., Figure 7). For a perfect fit, S is 0. Power laws are also described by two parameters: their slope α and a coefficient C. For clarity, we only present the slope values of the power laws. In the case of the two power laws fit, we also add the crossover area at which the power laws intersect. We call this parameter X_i. The steepest power law slope is termed α_2, while the less steep one is termed α_1. In the case of a single power law fit, the slope is referred to as α_2 if the slope is close to 2 or larger, or α_1 if the slope is closer to 1.

Details on the fitting method, including the identification of the range in which a power law is applicable (following Clauset et al., 2009), are given in the supporting information (Text S1).

4.2. Individual Fits

Data from each sample have been fitted both to power law and lognormal distributions (Figure 7 and Figure S1). All fits and associated distribution parameters can be found in Table 1. Median grain areas vary over 5 orders of magnitude, from 1.16 to 7.04×10^4 μm^2. The mean values of α_1 and α_2 over the whole data set are 1.05 ± 0.31 and 2.51 ± 0.48, respectively (errors are given by the standard deviation). The intersect value of the two power laws is approximately 3.0 times the median grain area (Figure 8).

The use of median area rather than the mean area of each sample is preferred because it is more robust with respect to extreme values, which could be caused by measurement uncertainties. The conversion from

Table 1
Properties of EBSD Maps and Fitting Parameters

Sample	Number of grains	Resolution (μm)	Median equivalent diameter (μm)	Mean area (μm²)	Median area (μm²)	μ	σ	S	α_1	α_2	X_i (μm²)
				Subset I							
Cor19 06 map 3 A	5,404	0.2	1.93E+00	5.96E+00	2.92E+00	0.79	1.31	0.306	1.02	2.46	7.63E+00
M02 8a map 1 A	2,493	0.5	8.24E+00	1.43E+02	5.33E+01	3.56	1.54	0.343	0.96	2.26	1.55E+02
M02 8a map 1 B	1,451	0.5	1.06E+01	1.49E+02	8.89E+01	3.95	1.32	0.197	0.82	3.56	3.54E+02
AF2 4 map 1 gt	3,291	0.35	2.43E+00	8.74E+00	4.66E+00	1.36	1.20	0.232	1.27	2.58	1.21E+01
AF2 4 map 2 gt	7,357	0.4	5.05E+00	4.04E+01	2.00E+01	2.76	1.24	0.149	1.05	3.51	1.23E+02
A16 011 map 2 pl	2,198	0.2	1.22E+00	1.73E+00	1.16E+00	0.05	0.96	0.110	1.39	2.73	2.55E+00
A16 011 map 8 pl	3,087	0.2	1.40E+00	2.14E+00	1.54E+00	0.37	0.79	0.186	1.12	3.35	2.94E+00
A16 013A map 3 pl	1,991	0.2	1.48E+00	3.29E+00	1.72E+00	0.51	1.10	0.128	1.08	2.31	3.85E+00
Al06 05a	3,733	Between 30 and 35	1.35E+02	2.14E+04	1.44E+04	9.03	1.20	0.382		2.63	
Al06 34	363		1.68E+02	3.38E+04	2.21E+04	9.95	0.90	0.209		2.49	
Al06 35	4,756		1.48E+02	3.24E+04	1.71E+04	8.82	1.69	0.293		2.33	
Al07 07	6,236		1.53E+02	2.35E+04	1.84E+04	9.39	0.93	0.308		3.35	
Am23b 01	3,118	3.2	1.69E+01	6.06E+02	2.25E+02	4.18	2.05	0.354		2.08	
B9006	3,285	1	4.92E+00	8.62E+01	1.90E+01	1.40	2.42	0.422		1.89	
B9010	5,070	1	5.17E+00	6.06E+01	2.10E+01	2.98	1.45	0.287		2.12	
B9014	5,830	0.7	3.53E+00	4.33E+01	9.80E+00	−0.34	2.79	0.499		1.86	
B9028	383	0.7	4.67E+00	9.49E+01	1.72E+01	2.87	1.95	0.227	1.42	2.07	2.35E+02
B9029	1,840	0.7	4.87E+00	3.95E+01	1.86E+01	2.88	1.22	0.128	1.40	3.24	1.31E+02
B9036	5,599	1	5.97E+00	9.93E+01	2.80E+01	3.23	1.62	0.308	1.58	2.26	1.81E+02
B9037	4,452	0.7	3.95E+00	5.28E+01	1.23E+01	1.76	1.84	0.704		1.97	
PT 889	1,053	Between 0.7 and 3	8.96E+00	1.01E+02	6.30E+01	4.11	1.09	0.101	0.84	2.92	1.65E+02
PT 892	640		1.26E+01	1.92E+02	1.25E+02	4.53	1.14	0.173	1.17	2.58	2.07E+02
PT 916 initial dry	527		2.79E+01	1.13E+03	6.12E+02	6.33	1.15	0.114	0.80	2.34	1.32E+03
PT 930 dry	1,692		1.38E+01	3.12E+02	1.49E+02	4.94	1.28	0.111	1.17	3.07	8.60E+02
PT 933 initial	585		3.17E+01	1.82E+03	7.90E+02	6.65	1.36	0.121	1.45		
PT 938 partial slip	673		2.58E+01	1.16E+03	5.22E+02	6.20	1.37	0.069	1.01	2.17	1.46E+03
PT 939	1,793		1.17E+01	1.99E+02	1.08E+02	4.68	1.10	0.184	0.98	2.98	3.76E+02
PT 952	1,238		1.63E+01	4.22E+02	2.08E+02	5.26	1.22	0.083	0.89	2.96	8.24E+02
PT 954	2,052		1.18E+01	2.09E+02	1.09E+02	4.58	1.26	0.111	0.95	2.97	4.01E+02
PT 966	1,258		7.87E+00	8.17E+01	4.86E+01	3.78	1.09	0.059	0.74	2.87	1.18E+02
PT 973	1,715		9.03E+00	1.34E+02	6.40E+01	4.06	1.28	0.132	0.78	2.40	1.27E+02
PT 976	643		1.67E+01	3.86E+02	2.18E+02	5.28	1.20	0.071	0.35	2.20	3.04E+02
NV05 123	2,051	>1/5 of mean diameter (between 10 and 100)	1.69E+02	5.11E+04	2.25E+04	9.49	1.59	0.250	1.71	2.23	4.27E+04
NV05 128	2,122		2.03E+02	8.27E+04	3.25E+04	10.23	1.44	0.214	1.21	2.45	1.32E+
NV05 129	3,526		1.43E+02	3.99E+04	1.60E+04	9.32	1.59	0.194	1.37	2.28	5.30E+04
NV05 161	1,579		2.99E+02	1.50E+05	7.04E+04	11.09	1.29	0.096	1.27	2.54	3.06E+05
NV05 162	1,477		2.59E+02	9.31E+04	5.25E+04	10.47	1.35	0.228		2.38	
NV05 165	2,886		2.26E+02	7.52E+04	4.00E+04	10.27	1.33	0.201	1.62	2.47	8.80E+04
NV05 168	1,803		1.64E+02	4.30E+04	2.13E+04	9.67	1.39	0.167	1.32	2.41	5.40E+04
NV05 171	1,843		2.63E+02	1.21E+05	5.44E+04	10.59	1.53	0.170	1.45	2.27	1.64E+05
BC05 101	1,458		1.39E+02	4.65E+04	1.52E+04	9.41	1.61	0.214	1.35	2.09	4.35E+04
BC05 123	1,122		2.49E+02	1.16E+05	4.86E+04	10.74	1.34	0.151	1.37	2.79	3.66E+05
				Subset II							
LE04 14 map 2 A	1,851	1.5	1.86E+01	9.99E+02	2.71E+02	5.45	1.75	0.189	0.97	2.18	1.21E+03
LE04 14 map 6 A	4,670	5	3.97E+01	2.60E+03	1.24E+03	7.06	1.18	0.534	1.28	2.47	3.42E+03
LE05 14 map 1 C	2,922	10	5.05E+01	5.72E+03	2.00E+03	6.79	1.91	0.290		2.03	
LE05 14 map 3 C	2,851	1	7.41E+00	7.25E+01	4.32E+01	2.97	1.52	0.297	0.44	2.47	4.83E+01
LEKD06 11A map 2	3,308	0.4	4.69E+00	5.02E+01	1.73E+01	1.84	2.03	0.283		2.05	
LEKD07 11B map 1	480	0.5	4.43E+00	3.46E+01	1.54E+01	2.62	1.42	0.148	1.02	2.19	4.04E+01
LECA16 11 map 1 f	1,318	0.2	1.53E+00	6.94E+00	1.85E+00	0.34	1.81	0.162	1.34	1.90	6.24E+00
LECA16 11 map 2 f	624	0.2	1.60E+00	7.42E+00	2.02E+00	0.54	1.76	0.140	1.29	1.84	6.22E+00
LECA16 11 map 1 s	899	0.2	2.04E+00	8.31E+00	3.28E+00	1.08	1.52	0.080	0.89	2.05	8.06E+00
LECA16 11 map 2 s	1,038	0.2	1.72E+00	1.32E+01	2.32E+00	0.73	1.97	0.145		1.70	

Note. Error due to binning is given in supporting information Table S1. EBSD = electron backscattered diffraction.
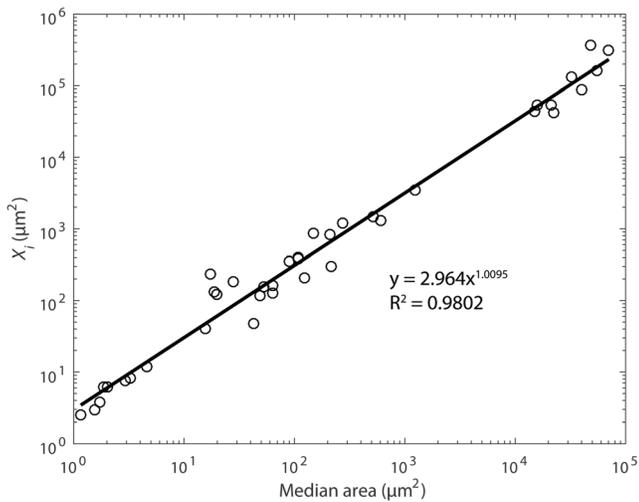
Figure 8. Median area versus intersection scale for the two power law parts. A similar figure can be obtained for mean area.

equivalent diameter to area is direct with the median ($D_{eq} = \sqrt{4A/\pi}$) but not with the mean. Finally, the median is a scaling parameter for lognormal distributions.

In the following, we present data from each subset of samples by groups. The fitting parameters associated with these groups are obtained from the mean value of the individual parameters. Errors are estimated based on maximum and minimum values as the number of sample in each group is too small for the standard deviation to be representative.

As samples are spread over several orders of magnitude in size, distributions are normalized to enable comparison. Two types of normalization are used: normalization to the median grain area (preferred if samples have a best fit to lognormal distributions) and normalization to the intersect value X_i (preferred if samples are best fitted by two power laws). In the case of fits using a single power law, the normalization is done using either median value normalization or normalization to 3.0 times the median grain size if samples are plotted with distributions normalized to X_i according to Figure 8. Plots representing all samples depending on their scaling behavior (two power laws, one power law, or lognormal) are given in Figures S2–S4 of the supporting information.

4.2.1. Subset I

Figure 9 shows the grain size distributions of the samples of subset I separated into the five groups defined in section 3.1. For each group a mean fit has been determined.

Samples undergoing grain size reduction during intermediate depth earthquakes display two power law parts with a mean α_1 of 1.1 $\pm_{0.3}^{0.3}$ (Figure 9a). Values of α_2 cluster around 2.5 $\pm_{0.2}^{0.3}$ but for three samples (M02-8a B, ÅF-4 map 2 and A16-011 map 8) collected in the immediate vicinity of the earthquake slip plane (represented by the pseudotachylites), for which the values are in the range 3.4–3.6.

All the hydrofractured samples (Padrón-Navarta et al., 2010) can be described by a single power law with a mean α_2 of 2.7 $\pm_{0.4}^{0.6}$ (Figure 9b).

Most of the kick-and-cook experiments and the natural equivalent (Druiventak et al., 2012; Trepmann et al., 2013) can be fitted by one power law with a mean value of α_2 of 2.0 $\pm_{0.2}^{0.2}$ (Figure 9c). Three kick-and-cook samples are better fitted to two power laws (B9028, B9029, and B9036). These three samples correspond to the ones that have undergone either the longest annealing times (144 hr for B9028 and B9029) or highest annealing temperatures (1100 °C for B9036). Their first power law part has a mean value of α_1 of 1.5 $\pm_{0.1}^{0.1}$, while their second parts follow the same power law as other samples.

Steady state torsion experiments from Tasaka et al. (2016) show a good fit to lognormal distribution with a value of σ close to 1.2 $\pm_{0.1}^{0.1}$ (Figure 9d). There is no clear difference in the distribution between wet and dry samples.

The case of mantle-deformed samples (Falus et al., 2011) is intermediate. A lognormal distribution with a σ value around 1.5 $\pm_{0.2}^{0.2}$ can fit all of the data except NV05-123, -162, and -165 with almost perfect data collapse when normalized to the median grain size (Figure 9e). However, a combination of two power laws fits all distributions well, including NV05-123, -162, and -165 with a mean α_1 of 1.3 $\pm_{0.1}^{0.1}$ and a mean α_2 of 2.4 $\pm_{0.3}^{0.4}$ (Figure 9f).

4.2.2. Subset II

Figure 10 shows the grain size distributions of the samples of subset II. Samples have been separated in three groups: mantle-deformed samples (zone A) from Dunkel, Austrheim, Renard, et al. (2017) and Dunkel, Austrheim, Ildefonse, and Jamtveit (2017); samples which can be fitted with a single power law comprising zone C samples from Dunkel, Austrheim, Renard, et al. (2017) and Dunkel, Austrheim, Ildefonse, and Jamtveit (2017; these were interpreted to have been deformed by brittle mechanisms during seismic slip) and sample LEKD06-11A; and the rest of the samples coming from two shear zones of variable width (LECA16-11 and LEKD07-11B).

Grain size distributions of mantle-deformed samples have been normalized to their median grain size area and can be fitted by lognormal distributions (Figure 10a). LE04-14 area 6 can be fitted with a σ value
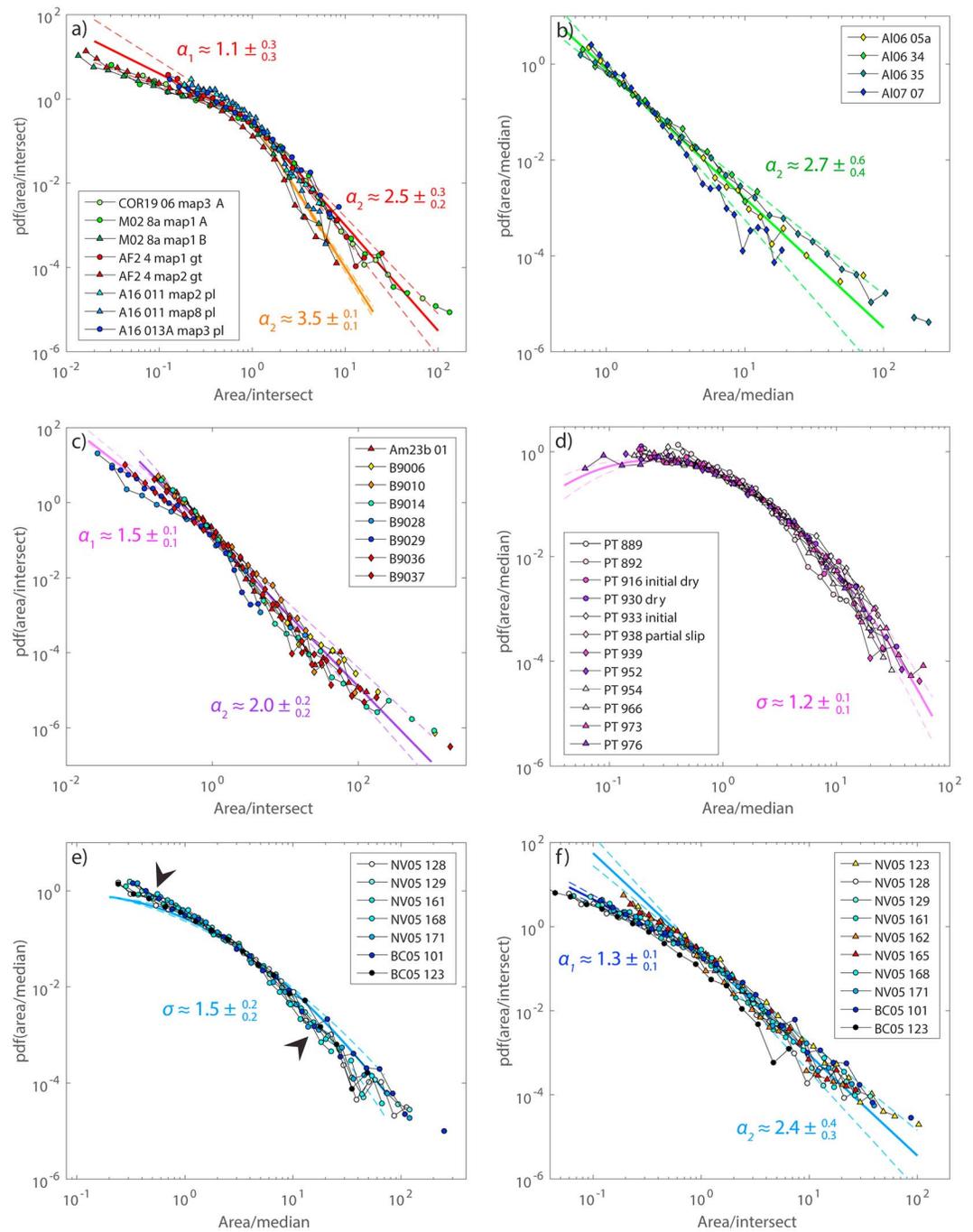
Figure 9. Grain size distributions of samples from Subset I. Mean values of α_1, α_2, or σ and their errors are indicated. Dashed lines indicate the error on the fitted slopes and σ. (a) Probability density functions (pdfs) of samples from intermediate depth earthquakes (Austrheim et al., 2017; Petley-Ragan et al., 2018) normalized to the intersection area of the two power laws. (b) pdf of samples from kick-and-cook experiments (Druiventak et al., 2012; Trepmann et al., 2013) normalized to the intersection area of the two power laws or 3.0 times their median grain size area when samples are fitted by only one power law. (c) pdf of hydrofractured samples (Padrón-Navarta et al., 2010) normalized to the median grain size area. (d) pdf of samples from steady state torsion experiments (Tasaka et al., 2016) normalized to the median area. (e and f) pdf of mantle-deformed samples (Falus et al., 2011) normalized to the median grain size area (e) and to the intersection area of the two power laws or 3.0 times their median grain size area when samples are fitted by a single power law (f). Black arrows in (e) indicate systematic deviations of the distributions from the lognormal law.
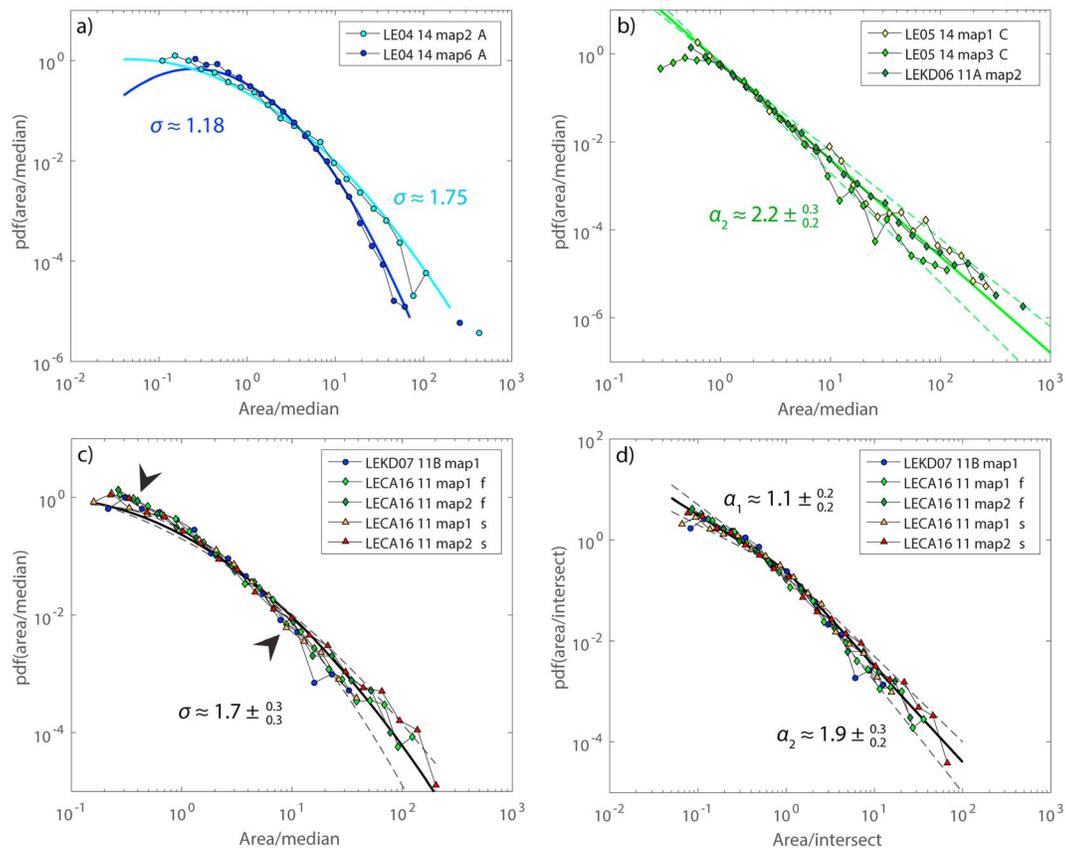
Figure 10. Grain size distributions of samples from Subset II. Dashed lines indicate the error of the fitted slopes and σ. (a) Mantle-deformed samples. (b) Fragmented wall rocks deformed by brittle deformation. (c) Samples from shear zones normalized to the median. (d) Samples from shear zones normalized to the scale where the two power laws intersect. Black arrows indicate systematic deviations of the distributions from the lognormal law.

around 1.2 similar to steady state torsion experiment values (Tasaka et al., 2016). LE04-14 area 2 is fitted by a higher σ value around 1.8.

Samples fitted by a single power law display α_2 values around $2.2 \pm_{0.2}^{0.3}$ (Figure 10b). Two power laws have been identified for LE05-14 area 3, but the one identified for small grain sizes spreads over less than an order of magnitude (Figure S1), and its slope is low (Table 1), indicating that this power law most probably corresponds to a lack of small grains due to measurement limitations. This sample is thus considered to be well represented by a single power law.

The remaining samples are presented normalized to their median grain size area (Figure 10c) and normalized by the intersect area obtained from fits with two power laws (Figure 10d). As for mantle-deformed samples from Falus et al., 2011, the normalization to the median grain size provides a very good data collapse. The grain size distributions obtained from samples LECA16-11 and LEKD07-11B display distributions close to lognormal distributions with sigma values around $1.7 \pm_{0.3}^{0.3}$. Normalization to the intersect value X_i returns a fairly good collapse, which fits a combination of two power laws with a mean α_1 of $1.1 \pm_{0.2}^{0.2}$ and a mean α_2 of $1.9 \pm_{0.2}^{0.3}$. There is no clear difference between fragmented (f) and sheared (s) domains in LECA16-11.

5. Grain Junctions

An analysis of the grain boundary angles at grain junctions reveals a very dominant peak around 120° for all the samples (Figure 11). This result is independent of grain size and indicates that grain boundary angles are highly influenced by surface energy reducing processes (such as growth) with no clear evidence for junctions controlled by hierarchical or conjugate fracture sets (cf. Iyer et al., 2008). However, the method used to determine angles may introduce some bias in the angle distributions as it leads to a finite smoothening of grain boundaries calculated from EBSD data.
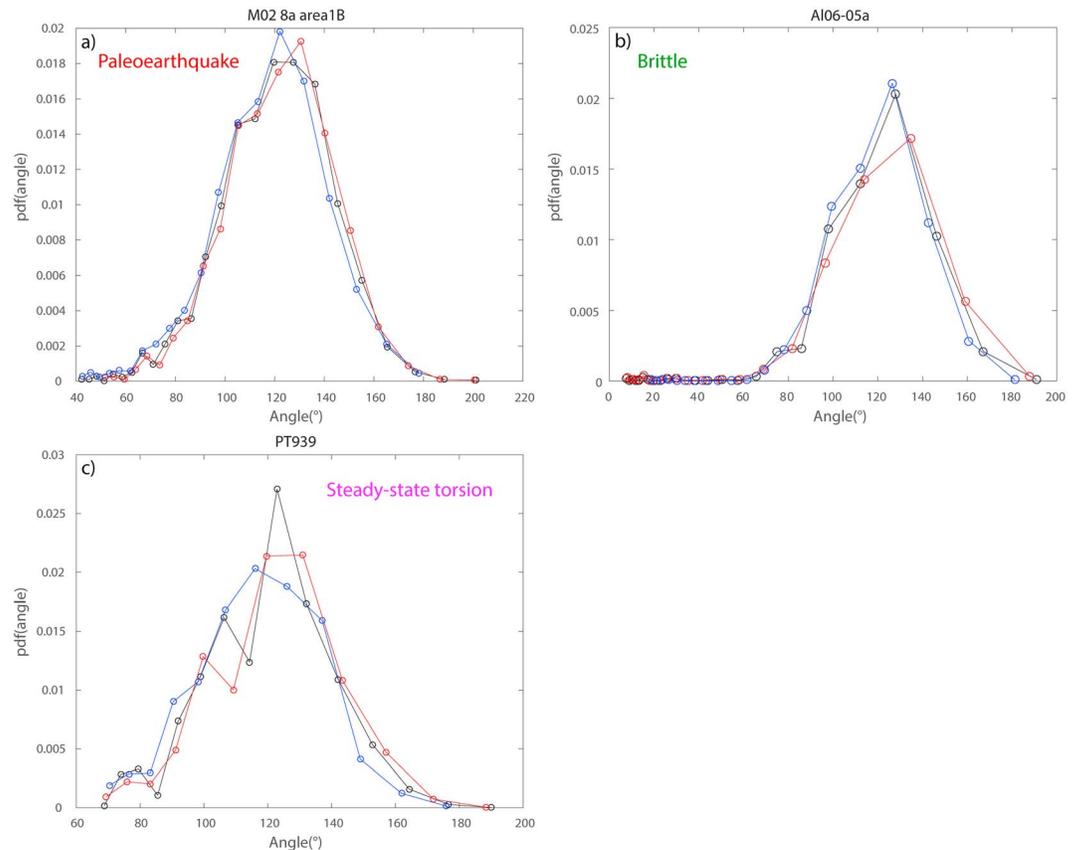
Figure 11. (a–c) Examples of angle distributions obtained from electron backscattered diffraction maps. The black curve is the distribution considering all the grains. The blue curve is the distribution obtained for grains smaller than the median grain size, and the red curve is the distribution obtained from grains bigger than the median grain size. In all cases, there is a maximum at around 120°, indicating a strong influence of surface energy reducing processes.

6. Stress and Strain Rates

Figure 12a shows all the data plotted in one diagram. Most data for grains smaller than the median value align along a single curve with a slope given by the first power law exponent. It can be approximated by $\text{pdf}(A) = 10^{-0.5}A^{-1}$. Exceptions include samples undergoing brittle fragmentation (the hydrofractured samples and zone C from Leka) and some samples from the kick-and-cook experiments of Trepmann et al. (2013), which follow a unique power law scaling at all scales. The grain sizes along this power law range from the resolution limit of the images (pixel size approximately 0.25 μm^2) to approximately 10^5 μm^2.

The largest grain populations, with median grain sizes around 10^5 μm^2, have been inferred to form at mantle conditions with expected strain rates on the order of 10^{-13}–10^{-15} s^{-1} (Pfiffner & Ramsay, 1982). Samples deformed experimentally at strain rates of 10^{-4}–10^{-5} s^{-1} show a median grain size variation in the range 10–800 μm^2, depending on the temperature and hence the stress level of the experiment, while seismically deformed samples are characterized by mean grain sizes below 10 μm^2. Figure 12b indicates that the strain rate roughly correlates with the median area to a power of -3.5 to -4.

7. Discussion

7.1. Distributions and Deformation Mechanics

The experiments of Tasaka et al. (2016) suggest that during dislocation creep, a steady state grain size distribution approaches lognormal scaling behavior, in agreement with previous assumptions. However, the fact that we find few lognormal distributions in the remaining natural samples indicates that steady state distributions are often not achieved during natural deformation.
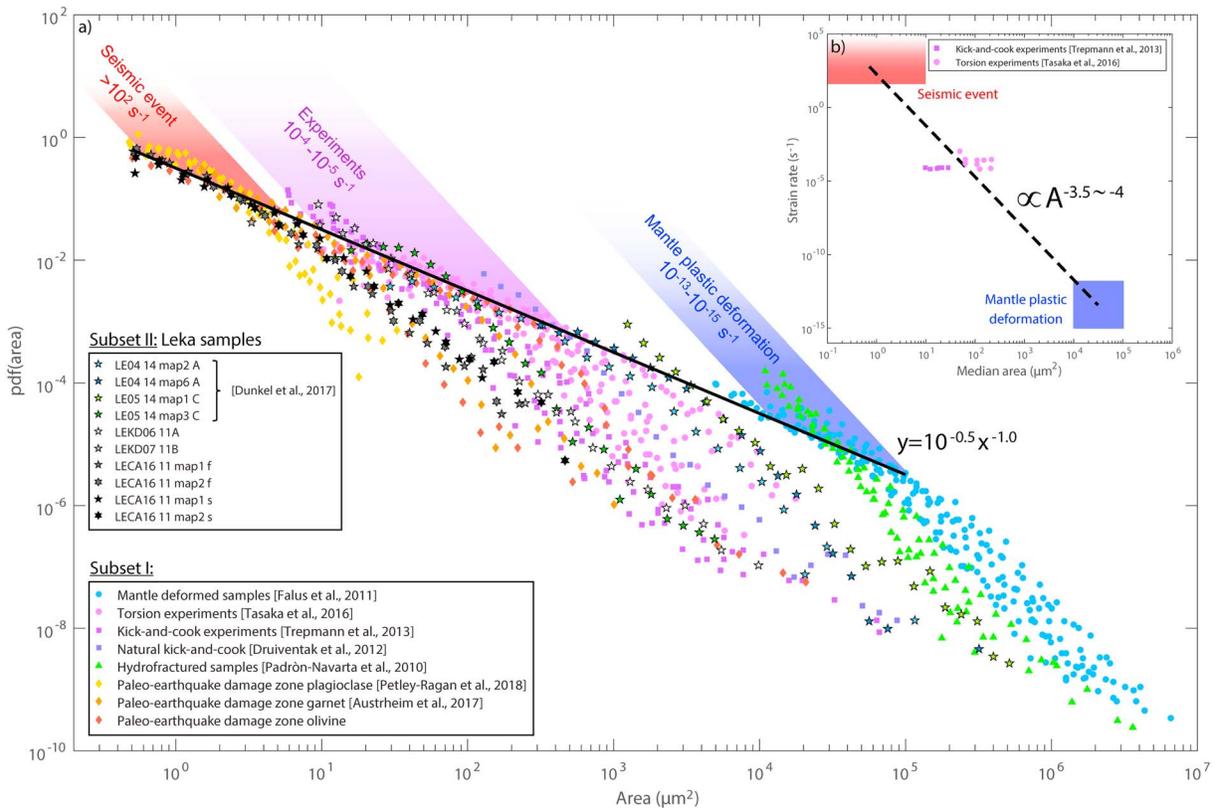
Figure 12. (a) Plot of the grain size distributions for all the studied samples. An envelope with a slope exponent of −1.0 can be identified. (b) Mantle-deformed samples (Falus et al., 2011), experimentally deformed samples (Tasaka et al., 2016; Trepmann et al., 2013), and samples from intermediate depth earthquakes (Austrheim et al., 2017; Petley-Ragan et al., 2018) allow constraints to be put on the negative correlation between strain rate and grain size. Note that the median grain size for samples from the kick-and-cook experiments are approximately 1 order of magnitude smaller than those from the steady state torsion experiments which were conducted at similar strain rates (10^{-4}–10^{-5} s^{-1}). This is due to the higher stress required to achieve a given strain rate for the lower-temperature (kick-and-cook) experiments.

Brittle fragmentation processes clearly lead to a power law grain size scaling, even in situations where there is very little shear deformation such as for the LE05 14 C sample from Leka (Dunkel, Austrheim, Ildefonse, & Jamtveit, 2017; Dunkel, Austrheim, Renard, et al., 2017). This also seems to hold in situations where the fragmentation takes place by low-temperature plasticity such as during the experiments of Druiventak et al. (2012) and Trepmann et al. (2013). Interestingly, kick-and-cook experiments carried out at high annealing temperature (1100 °C) or with long annealing times show a crossover to lower power law slopes for small grain sizes. This may suggest that the change from a large power law exponent to a smaller exponent is related to grain growth and recovery processes. This is also consistent with the scaling behavior observed for the seismically deformed garnets from the Bergen Arcs where growth of strain-free grains was reported to occur at the expense of dislocation-rich grains and subgrains (Austrheim et al., 2017). In that case the initial fragmentation process probably occurred by a combination of brittle mechanisms and low-temperature plasticity. We thus infer that the common situation observed in our data, where the grain size distribution fits a combination of two power laws, reflects the combination of a fragmentation process responsible for the steep slopes (given by α_2) and a recovery process that breaks the scaling toward more gentle slopes (α_1). In many situations, the fragmentation process precedes a later recovery and growth process, and thus, the final microstructure does not represent a steady state situation.

The use of a median grain size as a representative of the size distribution may still be useful as indicated by the close relation between the median and the power laws intersection (Figure 8), but one needs to be careful if using it to estimate paleostress.

The samples from the LOC show a wide range of grain size distributions, with median values in the range 1–10^3 μm^2. According to Figure 12b, this may reflect more than 10 orders of magnitude range in strain

rates. As mentioned above, the fragmented wall rock olivine next to what was interpreted as a seismic fault by Dunkel, Austrheim, Renard, et al. (2017) and Dunkel, Austrheim, Ildefonse, and Jamtveit (2017) shows a single power law. The mean grain size is approximately 7 μm^2, approaching the mean values for seismically deformed wall rock garnets and olivines from the Bergen Arcs and Corsica (1–8 μm^2). The initial mantle fabric shows a mostly lognormal distribution as expected, with mean grain sizes around 10^3 μm^2, which is 1–2 orders of magnitude smaller than the data from Falus et al. (2011) for mantle samples. The remaining data from Leka mainly show combination of two power laws, and the grain sizes are in most cases even smaller than for the wall rock olivines described by Dunkel, Austrheim, Renard, et al. (2017) and Dunkel, Austrheim, Ildefonse, and Jamtveit (2017), suggesting deformation at high stresses and strain rates. By comparison with the other data, it is reasonable to conclude that the microstructures in most of the studied samples of dunites from shear zones in the LOC reflect deformation at near-seismic strain rates. Since the sampling was biased to avoid samples rich in serpentine where fluids clearly played a key role during deformation, this does not imply that all deformation was related to earthquakes. It seems likely, however, that earthquakes were an important ingredient in the structural and metamorphic evolution of this ophiolite complex and perhaps even a key factor in introducing fluids into the system (cf. Jamtveit et al., 2018).

7.2. Model: Dislocation Patterning and Density Distributions

During crystal plastic deformation, the formation and size evolution of grains and subgrains at macroscopic scale are controlled at the microscopic scale by formation, movements, and annihilation of dislocations in the crystal lattice. Under stress, crystalline materials often develop a network of dislocations, which self-organize into cellular structures where dislocation-poor regions are bounded by cell walls with high dislocation densities. It has been observed experimentally (Raj & Pharr, 1986) that the average grain size of these cellular patterns (λ) is inversely proportional to the applied stress, similarly to what Twiss (1977) observed with grain and subgrain sizes. This is known as the *principle of similitude* (i.e., Gómez-García et al., 2006; Hähner, 1996a, 1996b; Hansen et al., 2001):

$$\frac{\sigma}{\mu} = K \frac{b}{\lambda}, \tag{1}$$

where σ is the applied stress, μ the shear modulus, b the magnitude of the Burgers vector, and K is an empirical constant. A phenomenological explanation of this experimental observation originates from Taylor's theory of plastic flow (Taylor, 1938). It defines the flow stress (σ_{plast}) as being proportional to the square root of the average density of dislocations:

$$\frac{\sigma_{plast}}{\mu} = \alpha b \sqrt{\rho}, \tag{2}$$

where ρ represents the number of dislocations intersecting a slip plane per unit area (2-D dislocation density) and α is a constant. Thus, from equations (1) and (2) the dislocations density ρ determines a typical length scale λ associated with the average size of the dislocation depleted regions. Hence, we can also interpret this length scale as a 1-D measure of the typical grain size, which means that the typical grain areas scale like the area of dislocation cells $A \sim \lambda^2$ which is inversely proportional to the dislocation density:

$$\lambda \sim \rho^{-1/2} \text{ or } A \sim \rho^{-1} \tag{3}$$

Dislocation formation, migration, and annihilation are adequately described by semiempirical equations. Using relation (3), we can connect the statistics of dislocation density fluctuations with the statistics of grain or subgrain sizes.

The main factors contributing to the time evolution of the mean dislocation density are the effective energy dissipation associated with plastic flow, $\frac{dE}{dt}$, and the driving force to stable dislocation configuration that minimize the interaction energy, $-\frac{dU}{d\rho}$ (Appendix A). This can be expressed by the following equation:

$$\dot{\rho} = -C_1 \ln(\rho) - C_1 + C_2 (\sigma_{ext} - \alpha b \mu \sqrt{\rho}) \dot{\varepsilon}, \tag{4}$$

where C_2 is a constant and $\dot{\varepsilon}$ is the strain rate. The term $-C_1 \ln(\rho) - C_1 = -C_1 \frac{d}{d\rho}(\rho \log \rho) = -\frac{dU}{d\rho}$ is the driving force associated with an average interaction potential $\rho \log \rho$ (Foreman, 1955; Appendix A), where C_1 is a constant depending on the elastic constants, for example, shear modulus and the Poisson ratio of the

medium. The effective energy dissipation term is $\dfrac{dE}{dt} = \sigma_{\text{eff}}\dot\varepsilon \approx (\sigma_{\text{ext}} - \alpha b\mu\sqrt\rho)\dot\varepsilon$ and has two sources: the external stress term and the plastic flow from the internal stress. The external stress component is related to the overall tectonic stress and considered as the unique source for dislocation generation, while plastic flow stress is related to the internal stress variations generated by the heterogeneous distribution of dislocations. Plastic flow stress and interactions between dislocations act to order and reduce dislocation density.

To study the distribution of the fluctuations in grain sizes that we observe in our samples, we propose a stochastic approach to equation (4) based on a modified version of the stochastic model by Hähner (1996a, 1996b). The basic idea is that collective interactions between dislocations lead to a fractal patterning and a power law distribution of grain sizes. In our case the global strain rate $\dot\varepsilon$ is expressed as the sum of an average deterministic value $\langle\dot\varepsilon\rangle$ representing an equilibrium value and a randomly fluctuating value η corresponding to fluctuations around the stationary average strain rate:

$$\dot\varepsilon = \langle\dot\varepsilon\rangle + \eta, \tag{5}$$

The noise term η originates from microscopic spatial heterogeneities of the strain rate and the evolving, complex dislocation structure. For simplicity, we assume that it has zero mean and is δ correlated with an autocorrelation function given by the following:

$$\langle\eta(t_1)\eta(t_2)\rangle = 2\zeta^2\delta(t_1 - t_2), \tag{6}$$

This means that the noise at different instants is uncorrelated and that the noise magnitude ζ increases with the occurrence of far from equilibrium strain rate values over the studied time interval.

The introduction of a stochastic strain rate into equation (4) leads to the following expression (Langevin equation) for the dislocation density variations:

$$\dot\rho = -C_1\ln(\rho) - C_1 + C_2\sigma_{\text{ext}}\langle\dot\varepsilon\rangle - C_2\alpha b\mu\sqrt\rho(\langle\dot\varepsilon\rangle + \eta) \tag{7}$$

The elastic energy stored in the presence of external stress couples with the average strain rate; hence, its dissipation rate gives the term $\sigma_{\text{ext}}\langle\dot\varepsilon\rangle$ in the time evolution of dislocation density. Noise stems solely from the stress component associated with plastic flow and thus internal deformation dynamics. This multiplicative noise term has a variance that increases linearly with ρ. The interpretation of this type of noise is nonunique, and a choice has to be made regarding which computation method to adopt. In our case, we use the Ito calculus (LeBlanc et al., 2013; Morita, 1981). We will not enter into the computational details of this method but simply discuss the consequences relevant to our model.

The evolution of the pdf of ρ, $P(\rho)$, is governed by the Fokker-Plank equation corresponding to equation (7) using Ito calculus for the multiplicative noise (Morita, 1981):

$$\frac{\partial P}{\partial t} = -\frac{\partial}{\partial\rho}\left[(a - C_1\ln(\rho) - C_3\sqrt\rho)P\right] + C_3{}^2\zeta^2\frac{\partial^2}{\partial\rho^2}[\rho P], \tag{8}$$

where $C_3 = C_2\alpha b\mu$ and a regroups all the constant terms affecting the variable ρ in (7). The steady state solution is given by the following (see Appendix B):

$$P(\rho) \sim \exp\left[-\frac{C_1}{2C_3{}^2\zeta^2}\left(\ln(\rho) + \frac{C_3{}^2\zeta^2}{C_1} - \frac{a}{C_1}\right)^2\right] \tag{9}$$

After a change of variable from dislocation density to grain size area using relation (3), that is, $P_A(A)dA = P(\rho)\,d\rho$, the distribution of grain areas $P_A(A)$ approaches a power law with a slope of -1 for large noise amplitude (large ζ^2) and a lognormal distribution for small noise amplitude (small ζ^2; Figure 13; see Appendix B).

The Ito calculus applies when we interpret the multiplicative noise as a punctuated process, which is a superposition of discrete events of a given magnitude that occur at random points in time (LeBlanc et al., 2013). When plastic motion is driven by dislocation motion, that is, when the global strain rate is determined
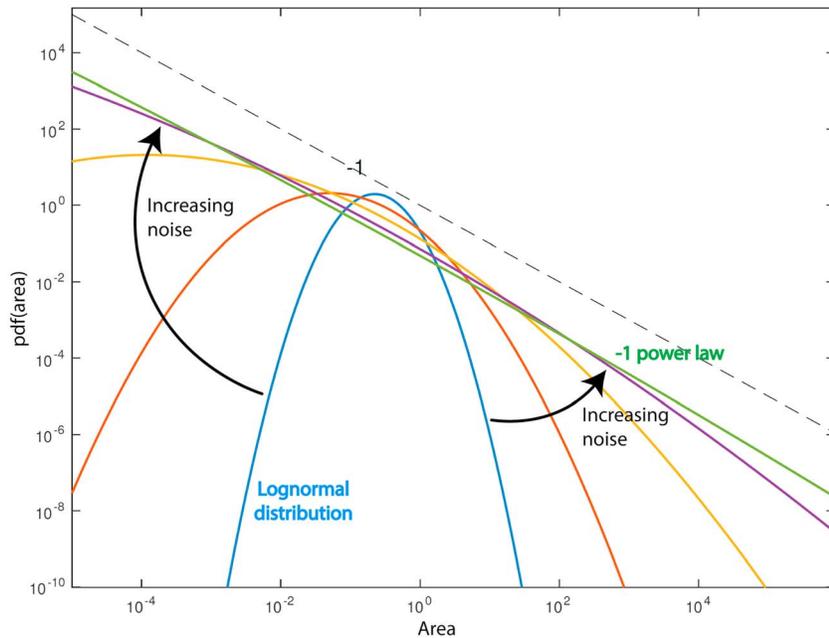
Figure 13. Area distribution for different values of the noise parameter $C_3^2 \zeta^{-2}$, showing that with increasing noise, the distribution changes from lognormal to power law.

by the dislocation dynamics (rate of dislocation formation, storage, annihilation, etc.), the global strain rate can be approximated by a superposition of nonoverlapping *slip avalanches*:

$$\dot{\varepsilon} = \textstyle\sum_i \widehat{\varepsilon_i} G(t - t_i), \tag{10}$$

$\widehat{\varepsilon_i}$ is the strain accumulated during the slip event i happening within a short time interval (T) centered at t_i, and $G(t - t_i)$ is a sharply peaked function (or time kernel). The average time lag between slip events and the average strain increment are denoted by τ and $\widehat{\varepsilon}$, respectively. The noise arises from variations of $\widehat{\varepsilon_i}$ and t_i relative to values $\widehat{\varepsilon}$, τ, and T. The mean ($\langle \dot{\varepsilon} \rangle$) and standard deviation (noise amplitude, ζ^2) of the strain rate can be determined from the parameters $\widehat{\varepsilon}$, τ, and T (Hähner, 1996b):

$$\langle \dot{\varepsilon} \rangle = \frac{\widehat{\varepsilon}}{\tau} \tag{11}$$

$$\zeta^2 = \frac{\widehat{\varepsilon}^2}{\sqrt{2\pi}} \frac{1}{\tau T} \tag{12}$$

For small noise amplitude ($\zeta^2 \ll \langle \dot{\varepsilon} \rangle^2$), relations (11) and (12) lead to $\tau \ll T$, meaning that dislocations are almost constantly slipping to accommodate the strain. Since we assume steady state, the rate of dislocation reactions reducing the dislocation density is of the same order as the rate of dislocation multiplication. In this case the steady state solution to equation (8) indicates the grain size distribution will be lognormal (Figure 13).

In the case of large noise amplitude, $\tau \gg T$. This means that slips happen during very short time steps compared to the overall deformation. Deformation is happening discontinuously and dislocation self-organization is very efficient compared to strain rate. In this case the steady state solution to equation (8) indicates that the grain size distribution is a power law of slope -1 (Figure 13). As the variance of the noise is positively correlated with the dislocation density, this case implies high dislocation densities in the limits of our model.

During deformation, noise can have various origins, including heterogeneities already present in the rock (occurrence of different phases, grain sizes, modifying locally the strength of the rock), but the main controlling parameter is the rate of dislocation storage and healing compared to strain rate. If the self-organization of dislocations is fast compared to deformation strain rate, leading to discontinuous strain accommodation by the dislocations, a distribution of grain areas is expected to follow a power law with a

slope of −1. If the self-organization of dislocations is fast enough to control the deformation strain rate but of the same order of magnitude as the deformation rate, a lognormal distribution is expected for grain size area distribution. The model presented above assumes dislocation controlled deformation. Hence, it does not describe the situation where the strain rate is too fast to be accommodated by dislocation motion. Based on our data and previous studies of grain size distributions of samples fragmented by brittle mechanisms (e.g., An & Sammis, 1994; Billi, 2005; Heilbronner & Keulen, 2006), a power law distribution with a slope around −2 would then be expected.

For a given rate of dislocation self-organization, the −1 power law case would be expected for very slow strain rates eventually down to 0 (healing) and high dislocation density (which could be the normal situation after a seismic event), while the lognormal case would be expected for strain rates of the same order of magnitude as the dislocation dynamics with efficient organization of the dislocations and thus lower dislocation density in bulk. Power laws with larger slopes are expected for high strain rates. The lognormal distribution, as we observe in steady state torsion experiments and some mantle-deformed samples, could be considered as the *equilibrium* one which can be used for paleostress estimates as it is expected when the dislocation dynamics operate at rates comparable to the strain rate.

The steady state leading to the −1 slope is not a long-lived steady state as it requires a high dislocation density, which may not last long under conditions where strain rate is slow and recovery processes active. In between events leading to these high dislocation densities and discontinuous deformation, the regime may progressively tend toward a regime of more continuous deformation and thus lognormal distribution. This could explain the intermediate distribution of most of our samples.

The envelope (line with −1 slope) shown in Figure 12a may reflect the equilibrium lognormal shape towards which all the distributions eventually should converge. Indeed, the envelope created by lognormal distributions of similar σ but spread over a large range of μ values follows a relation proportional to a power law of slope −1. In the case of σ close to 1.2, the proportionality coefficient is close to $10^{-0.5}$, as observed.

The strain rate is externally imposed by tectonic stress, but it is interesting to identify what controls how fast dislocations can organize themselves. Dislocation slip events are often considered as equivalent to chemical reactions, which means that the two main parameters controlling their rates are temperature and dislocation concentration. Higher temperatures and concentrations lead to higher reaction rates. For a deforming polycrystalline rock, the temperature is the same for all grain sizes; thus, dislocation density is controlling the *reaction rates* of the dislocations. The dislocation self-organization will be faster in small grains than in large grains, and different noise conditions may apply depending on grain size.

8. Summary

In this paper we presented a unique set of grain size distributions of olivine-dominated rocks deformed over a wide range of strain rates from slow mantle flow to seismic fragmentation. We observe a surprisingly coherent behavior for most natural samples, with a power law probability distribution function of areas near −1 for the smallest grain fraction, and a steeper slope (in most cases in the range −2 to −2.5) for the larger grain fraction. Convincing lognormal distributions across scales were only observed for samples experimentally deformed at high temperatures (and designed to achieve steady state distributions) and some mantle-deformed natural samples. Simple power law distribution with a single exponent was only observed for natural samples deformed by brittle mechanisms and experimentally deformed samples interpreted to have deformed by low-temperature plasticity.

Most natural samples show a clear cross over in scaling behavior near the median grain size and show a good data collapse for small grains when normalized to the crossover scale. The associated power law slope of approximately −1 indicates that a common process controls grain size behavior. We present a model that explains how such scaling behavior may arise in the dislocation creep regime from the competition between the rates involved in the dislocation dynamics and the strain rate.

The common departure from lognormal distributions suggests that naturally deformed samples often display a grain size distribution that reflects a deformation history far from a steady state scenario and probably arises due to deformation under changing stress and strain rates as previously proposed by Trepmann and Stöckhert (2003) and Trepmann et al. (2007).

Appendix A: Interaction Energy Contribution to Dislocation Density Variations

The average energy of dislocation due to the interaction with its nearest neighbor is (Foreman, 1955) as follows:

$$u(\lambda) \sim -\mu b^2 \frac{1 - \nu/2}{4\pi(1-\nu)} \ln\left(\frac{\lambda}{b}\right) \tag{A1}$$

Assuming that all the dislocations have approximately the same interaction energy u and using relation (3), the total interaction energy for a configuration of dislocations with density ρ is given as follows:

$$U(\rho) \sim \rho u\left(\rho^{-1/2}\right) \sim -\mu b^2 \frac{1 - \nu/2}{4\pi(1-\nu)} \rho \ln\left(\frac{1}{b\sqrt{\rho}}\right), \tag{A2}$$

The driving force obtained from minimizing dislocation interactions energy is then

$$-\frac{dU}{d\rho} = -C_1 \ln(\rho) - C_1, \text{ where } 2C_1 = \mu b^2 \frac{1 - \nu/2}{4\pi(1-\nu)} \tag{A3}$$

Appendix B: Solution to Fokker-Plank Equation for Dislocation Density

The probability density $P(\rho,t)$ for the dislocation density is obtained by writing the Fokker-Plank equation related to equation (7) in its Ito form (Morita, 1981):

$$\frac{\partial P}{\partial t} = -\frac{\partial}{\partial \rho}\left[\left(a - C_1 \ln(\rho) - C_3\sqrt{\rho}\right)P\right] + C_3^2\zeta^2 \frac{\partial^2}{\partial \rho^2}[\rho P] \tag{B1}$$

The stationary solution satisfies the following:

$$\frac{\partial P}{\partial \rho} + P = \frac{1}{C_3^2\zeta^2}\left(a - C_1 \ln(\rho) - C_3\sqrt{\rho}\right)P \tag{B2}$$

$$\frac{dP}{P} = \left(-1 + \frac{a}{C_3^2\zeta^2}\right)\frac{d\rho}{\rho} - \frac{C_1}{C_3^2\zeta^2}\ln(\rho)\frac{d\rho}{\rho} - \frac{1}{C_3\zeta^2}\sqrt{\rho}\frac{d\rho}{\rho} \tag{B3}$$

$$P(\rho) \sim \exp\left[\left(-1 + \frac{a}{C_3^2\zeta^2}\right)\ln(\rho) - \frac{C_1}{C_3^2\zeta^2}\ln^2(\rho)\right] \tag{B4}$$

$$P(\rho) \sim \exp\left[-\left(\sqrt{\frac{C_1}{2C_3^2\zeta^2}}\ln(\rho) - \sqrt{\frac{C_3^2\zeta^2}{2C_1}}\left(-1 + \frac{a}{C_3^2\zeta^2}\right)\right)^2\right] \tag{B5}$$

$$P(\rho) \sim \exp\left[-\frac{C_1}{2C_3^2\zeta^2}\left(\ln(\rho) - \frac{C_3^2\zeta^2}{C_1}\left(-1 + \frac{a}{C_3^2\zeta^2}\right)\right)^2\right] \tag{B6}$$

$$P(\rho) \sim \exp\left[-\frac{C_1}{2C_3^2\zeta^2}\left(\ln(\rho) + \frac{C_3^2\zeta^2}{C_1} - \frac{a}{C_1}\right)^2\right] \tag{B7}$$

Or with the change of variable from dislocation density to area $P_A(A)dA = P(\rho)d\rho = A^{-2}P(A^{-1})$,

$$P_A(A) \sim A^{-2} \exp\left[-\frac{C_1}{2C_3^2\zeta^2}\left(-\ln(A) + \frac{C_3^2\zeta^2}{C_1} - \frac{a}{C_1}\right)^2\right] \tag{B8}$$

In the case of large noise amplitude $C_3^2\zeta^2 \gg C_1$,

$$P_A(A) \sim A^{-1} \tag{B9}$$

In the case of small noise amplitude $C_3^2\zeta^2 \ll C_1$,

$$P_A(A) \sim A^{-2}\exp\left[-\frac{C_1}{2C_3^2\zeta^2}\left(\ln(A) + \frac{a}{C_1}\right)^2\right] \tag{B10}$$

For illustration of the solution with various noise values see Figure 13.

References

An, L.-J., & Sammis, C. G. (1994). Particle size distribution of cataclastic fault materials from Southern California: A 3-D study. *Pure and Applied Geophysics*, *143*(1–3), 203–227. https://doi.org/10.1007/BF00874329

Andersen, T. B., & Austrheim, H. (2006). Fossil earthquakes recorded by pseudotachylytes in mantle peridotite from the Alpine subduction complex of Corsica. *Earth and Planetary Science Letters*, *242*(1–2), 58–72. https://doi.org/10.1016/j.epsl.2005.11.058

Austin, N. J., & Evans, B. (2007). Paleowattmeters: A scaling relation for dynamically recrystallized grain size. *Geology*, *35*(4), 343–346. https://doi.org/10.1130/G23244A.1

Austrheim, H., Dunkel, K. G., Plümper, O., Ildefonse, B., Liu, Y., & Jamtveit, B. (2017). Fragmentation of wall rock garnets during deep crustal earthquakes. *Science Advances*, *3*(2), e1602067. https://doi.org/10.1126/sciadv.1602067

Austrheim, H., Erambert, M., & Boundy, T. M. (1996). Garnets recording deep crustal earthquakes. *Earth and Planetary Science Letters*, *139*(1–2), 223–238. https://doi.org/10.1016/0012-821X(95)00232-2

Bachmann, F., Hielscher, R., & Schaeben, H. (2010). Texture analysis with MTEX—Free and open source software toolbox. *Solid State Phenomena*, *160*, 63–68. https://doi.org/10.4028/www.scientific.net/SSP.160.63

Bachmann, F., Hielscher, R., & Schaeben, H. (2011). Grain detection from 2d and 3d EBSD data—Specification of the MTEX algorithm. *Ultramicroscopy*, *111*(12), 1720–1733. https://doi.org/10.1016/j.ultramic.2011.08.002

Billi, A. (2005). Grain size distribution and thickness of breccia and gouge zones from thin (<1 m) strike-slip fault cores in limestone. *Journal of Structural Geology*, *27*(10), 1823–1837. https://doi.org/10.1016/j.jsg.2005.05.013

Clauset, A., Shalizi, C., & Newman, M. (2009). Power-law distributions in empirical data. *SIAM Review*, *51*(4), 661–703. https://doi.org/10.1137/070710111

Cross, A. J., Ellis, S., & Prior, D. J. (2015). A phenomenological numerical approach for investigating grain size evolution in ductiley deforming rocks. *Journal of Structural Geology*, *76*, 22–34. https://doi.org/10.1016/j.jsg.2015.04.001

De Bresser, J. H. P., Ter Heege, J. H., & Spiers, C. J. (2001). Grain size reduction by dynamic recrystallization: Can it result in major theological weakening? *International Journal of Earth Sciences*, *90*(1), 28–45. https://doi.org/10.1007/s005310000149

Doherty, R. D., Hughes, D. A., Humphreys, F. J., Jonas, J. J., Jensen, D. J., Kassner, M. E., et al. (1997). Current issues in recrystallization: A review. *Materials Science and Engineering A*, *238*(2), 219–274. https://doi.org/10.1016/S0921-5093(97)00424-3

Druiventak, A., Matysiak, A., Renner, J., & Trepmann, C. A. (2012). Kick-and-cook experiments on peridotite: Simulating coseismic deformation and post-seismic creep. *Terra Nova*, *24*(1), 62–69. https://doi.org/10.1111/j.1365-3121.2011.01038.x

Druiventak, A., Trepmann, C. A., Renner, J., & Hanke, K. (2011). Low-temperature plasticity of olivine during high stress deformation of peridotite at lithospheric conditions—An experimental study. *Earth and Planetary Science Letters*, *311*(3–4), 199–211. https://doi.org/10.1016/j.epsl.2011.09.022

Drury, M., & Urai, J. (1990). Deformation-related recrystallization processes. *Tectonophysics*, *172*(3–4), 235–253. https://doi.org/10.1016/0040-1951(90)90033-5

Dunkel, K. G., Austrheim, H., Ildefonse, B., & Jamtveit, B. (2017). Transfer of olivine crystallographic orientation through a cycle of serpentinisation and dehydration. *Contributions to Mineralogy and Petrology*, *172*(8), 64. https://doi.org/10.1007/s00410-017-1378-5

Dunkel, K. G., Austrheim, H., Renard, F., Cordonnier, B., & Jamtveit, B. (2017). Localized slip controlled by dehydration embrittlement of partly serpentinized dunites, Leka Ophiolite Complex, Norway. *Earth and Planetary Science Letters*, *463*, 277–285. https://doi.org/10.1016/j.epsl.2017.01.047

Dunning, G. R., & Pedersen, R. B. (1988). U/Pb ages of ophiolites and arc-related plutons of the Norwegian Caledonides: Implications for the development of Iapetus. *Contributions to Mineralogy and Petrology*, *98*(1), 13–23. https://doi.org/10.1007/BF00371904

Falus, G., Tommasi, A., & Soustelle, V. (2011). The effect of dynamic recrystallization on olivine crystal preferred orientations in mantle xenoliths deformed under varied stress conditions. *Journal of Structural Geology*, *33*(11), 1528–1540. https://doi.org/10.1016/j.jsg.2011.09.010

Feltham, P. (1957). Grain growth in metals. *Acta Metallurgica*, *5*(2), 97–105. https://doi.org/10.1016/0001-6160(57)90136-0

Foreman, A. J. E. (1955). Dislocation energies in anisotropic crystals. *Acta Metallurgica*, *3*(4), 322–330. https://doi.org/10.1016/0001-6160(55)90036-5

Furnes, H., Pedersen, R. B., & Stillman, C. J. (1988). The Leka Ophiolite Complex, central Norwegian Caledonides: Field characteristics and geotectonic significance. *Journal of the Geological Society*, *145*(3), 401–412. https://doi.org/10.1144/gsjgs.145.3.0401

Gómez-García, D., Devincre, B., & Kubin, L. P. (2006). Dislocation patterns and the similitude principle: 2.5D mesoscale simulations. *Physical Review Letters*, *96*(12), 12,5503. https://doi.org/10.1103/PhysRevLett.96.125503

Hähner, P. (1996a). A theory of dislocation cell formation based on stochastic dislocation dynamics. *Acta Materialia*, *44*(6), 2345–2352. https://doi.org/10.1016/1359-6454(95)00364-9

Hähner, P. (1996b). On the foundations of stochastic dislocation dynamics. *Applied Physics A*, *62*(5), 473–481. https://doi.org/10.1007/BF01567120

Hansen, L. N., Zimmerman, M. E., & Kohlstedt, D. L. (2011). Grain boundary sliding in San Carlos olivine: Flow law parameters and crystallographic-preferred orientation. *Journal of Geophysical Research*, *116*, B08201. https://doi.org/10.1029/2011JB008220

Hansen, N., Huang, X., & Hughes, D. A. (2001). Microstructural evolution and hardening parameters. *Materials Science and Engineering A*, *317*(1–2), 3–11. https://doi.org/10.1016/S0921-5093(01)01191-1

Heilbronner, R., & Keulen, N. (2006). Grain size and grain shape analysis of fault rocks. *Tectonophysics*, *427*(1–4), 199–216. https://doi.org/10.1016/j.tecto.2006.05.020

Hielscher, R., & Schaeben, H. (2008). A novel pole figure inversion method: Specification of the MTEX algorithm. *Journal of Applied Crystallography*, *41*(6), 1024–1037. https://doi.org/10.1107/S0021889808030112

Iyer, K., Jamtveit, B., Mathiesen, J., Malthe-Sørenssen, A., & Feder, J. (2008). Reaction-assisted hierarchical fracturing during serpentinization. *Earth and Planetary Science Letters*, *267*(3–4), 503–516. https://doi.org/10.1016/j.epsl.2007.11.060

Jamtveit, B., Ben-Zion, Y., Renard, F., & Austrheim, H. (2018). Earthquake-induced transformation of the lower crust. *Nature*, *556*(7702), 487–491. https://doi.org/10.1038/s41586-018-0045-y

Jung, H., & Karato, S. I. (2001). Effects of water on dynamically recrystallized grain-size of olivine. *Journal of Structural Geology*, *23*(9), 1337–1344. https://doi.org/10.1016/S0191-8141(01)00005-0

Jung, S., Jung, H., & Austrheim, H. (2014). Characterization of olivine fabrics and mylonite in the presence of fluid and implications for seismic anisotropy and shear localization. *Earth, Planets and Space*, *66*(1), 46. https://doi.org/10.1186/1880-5981-66-46

Kile, D. E., Eberl, D. D., Hoch, A. R., & Reddy, M. M. (2000). An assessment of calcite growth mechanisms based on crystal size distributions. *Geochimica et Cosmochimica Acta*, *64*(17), 2937–2950. https://doi.org/10.1016/S0016-7037(00)00394-X

Kirkpatrick, J. D., & Rowe, C. D. (2013). Disappearing ink: How pseudotachylytes are lost from the rock record. *Journal of Structural Geology*, *52*, 183–198. https://doi.org/10.1016/j.jsg.2013.03.003

Kühn, A., Glodny, J., Iden, K., & Austrheim, H. (2000). Retention of Precambrian Rb/Sr phlogopite ages through Caledonian eclogite facies metamorphism, Bergen Arc Complex, W-Norway. *Lithos*, *51*(4), 305–330. https://doi.org/10.1016/S0024-4937(99)00067-5

Leblanc, M., Angheluta, L., Dahmen, K., & Goldenfeld, N. (2013). Universal fluctuations and extreme statistics of avalanches near the depinning transition. *Physical Review E*, *87*(2), 022126. https://doi.org/10.1103/PhysRevE.87.022126

Linckens, J., Zulauf, G., & Hammer, J. (2016). Experimental deformation of coarse-grained rock salt to high strain. *Journal of Geophysical Research: Solid Earth*, *121*, 6150–6171. https://doi.org/10.1002/2016JB012890

Magott, R., Fabbri, O., & Fournier, M. (2016). Subduction zone intermediate-depth seismicity: Insights from the structural analysis of Alpine high-pressure ophiolite-hosted pseudotachylyte (Corsica, France). *Journal of Structural Geology*, *87*, 95–114. https://doi.org/10.1016/j.jsg.2016.04.002

Morita, T. (1981). On the interpretation of multiplicative white noise. *Physics Letters A*, *82*(5), 215–217. https://doi.org/10.1016/0375-9601(81)90187-0

Nicolas, A., & Christensen, N. I. (1987). Formation of anisotropy in upper mantle peridotites—A review. In K. Fuchs & C. Froidevaux (Eds.), *Composition, structure and dynamics of the lithosphere-asthenosphere system* (pp. 111–123). Washington, DC: American Geophysical Union. https://doi.org/10.1029/GD016p0111

Padrón-Navarta, J. A., Tommasi, A., Garrido, C. J., Sánchez-Vizcaíno, V. L., Gómez-Pugnaire, M. T., Jabaloy, A., & Vauchez, A. (2010). Fluid transfer into the wedge controlled by high-pressure hydrofracturing in the cold top-slab mantle. *Earth and Planetary Science Letters*, *297*(1–2), 271–286. https://doi.org/10.1016/j.epsl.2010.06.029

Petley-Ragan, A., Dunkel, K. G., Austrheim, H., Ildefonse, B., & Jamtveit, B. (2018). Microstructural records of intermediate-depth earthquakes and associated fluid-driven metamorphism of plagioclase-rich granulites. *Journal of Geophysical Research: Solid Earth*, *123*, 3729–3746. https://doi.org/10.1029/2017JB015348

Pfiffner, O. A., & Ramsay, J. G. (1982). Constraints on geological strain rates: Arguments from finite strain states of naturally deformed rocks. *Journal of Geophysical Research*, *87*, 311–321. https://doi.org/10.1029/JB087iB01p00311

Raj, S. V., & Pharr, G. M. (1986). A compilation and analysis of data for the stress dependence of the subgrain size. *Materials Science and Engineering*, *81*, 217–237. https://doi.org/10.1016/0025-5416(86)90265-X

Ricard, Y., & Bercovici, D. (2009). A continuum theory of grain size evolution and damage. *Journal of Geophysical Research*, *114*, B01204. https://doi.org/10.1029/2007JB005491

Roberts, D., Nordgulen, Ø., & Melezhik, V. (2007), The uppermost allochthon in the Scandinavian Caledonides: From a Laurentian ancestry through Taconian orogeny to Scandian crustal growth on Baltica. In R. D. Hatcher, Jr., M. P. Carlson, J. H. McBride, & J. R. Martínez Catalán (Eds.), *4-D framework of continental crust* (mem. 200, pp. 357–377). Boulder, Colorado: Geological Society of America. https://doi.org/10.1130/2007.1200(18)

Rozel, A., Ricard, Y., & Bercovici, D. (2011). A thermodynamically self-consistent damage equation for grain size evolution during dynamic recrystallization. *Geophysical Journal International*, *184*(2), 719–728. https://doi.org/10.1111/j.1365-246X.2010.04875.x

Sammis, C., King, G., & Biegel, R. (1987). The kinematics of gouge deformation. *Pure and Applied Geophysics*, *125*(5), 777–812. https://doi.org/10.1007/BF00878033

Sammis, C. G., & Ben-Zion, Y. (2008). Mechanics of grain-size reduction in fault zones. *Journal of Geophysical Research*, *113*, B02306. https://doi.org/10.1029/2006JB004892

Sibson, R. H. (1975). Generation of pseudotachylyte by ancient seismic faulting. *Geophysical Journal International*, *43*(3), 775–794. https://doi.org/10.1111/j.1365-246X.1975.tb06195.x

Stipp, M., Stunitz, H., Heilbronner, R., & Schmid, S. M. (2002). Dynamic recrystallization of quartz: Correlation between natural and experimental conditions. In S. DeMeer, M. R. Drury, J. H. P. DeBresser, & G. M. Pennock (Eds.), *Deformation mechanisms, rheology and tectonics: Current status and future perspectives* (pp. 171–190). Bath: Geological Soc Publishing House. https://doi.org/10.1144/GSL.SP.2001.200.01.11

Stipp, M., Tullis, J., Scherwath, M., & Behrmann, J. H. (2010). A new perspective on paleopiezometry: Dynamically recrystallized grain size distributions indicate mechanism changes. *Geology*, *38*(8), 759–762. https://doi.org/10.1130/G31162.1

Tasaka, M., Zimmerman, M. E., & Kohlstedt, D. L. (2016). Evolution of the rheological and microstructural properties of olivine aggregates during dislocation creep under hydrous conditions. *Journal of Geophysical Research: Solid Earth*, *121*, 92–113. https://doi.org/10.1002/2015JB012134

Taylor, G. I. (1938). Plastic strain in metals. *Journal of the Institute of Metals*, *62*, 307–324.

Titus, S. J., Fossen, H., Pedersen, R. B., Vigneresse, J. L., & Tikoff, B. (2002). Pull-apart formation and strike-slip partitioning in an obliquely divergent setting, Leka ophiolite, Norway. *Tectonophysics*, *354*(1–2), 101–119. https://doi.org/10.1016/S0040-1951(02)00293-7

Tommasi, A., Mainprice, D., Canova, G., & Chastel, Y. (2000). Viscoplastic self-consistent and equilibrium-based modeling of olivine lattice preferred orientations: Implications for the upper mantle seismic anisotropy. *Journal of Geophysical Research*, *105*, 7893–7908. https://doi.org/10.1029/1999JB900411

Trepmann, C. A., Renner, J., & Druiventak, A. (2013). Experimental deformation and recrystallization of olivine—Processes and timescales of damage healing during postseismic relaxation at mantle depths. *Solid Earth*, *4*(2), 423–450. https://doi.org/10.5194/se-4-423-2013

Trepmann, C. A., & Stöckhert, B. (2003). Quartz microstructures developed during non-steady state plastic flow at rapidly decaying stress and strain rate. *Journal of Structural Geology*, *25*(12), 2035–2051. https://doi.org/10.1016/S0191-8141(03)00073-7

Trepmann, C. A., Stöckert, B., Dorner, D., Moghadam, R. H., Küster, M., & Röller, K. (2007). Simulating coseismic deformation of quartz in the middle crust and fabric evolution during postseismic stress relaxation—An experimental study. *Tectonophysics*, *442*(1–4), 83–104. https://doi.org/10.1016/j.tecto.2007.05.005

Twiss, R. J. (1977). Theory and applicability of a recrystallized grain size paleopiezometer. In M. Wyss (Ed.), *Stress in the Earth* (pp. 227–244). Birkhäuser, Basel: Contributions to Current Research in Geophysics (CCRG). https://doi.org/10.1007/978-3-0348-5745-1_13

Van der Wal, D., Chopra, P., Drury, M., & Gerald, J. F. (1993). Relationships between dynamically recrystallized grain size and deformation conditions in experimentally deformed olivine rocks. *Geophysical Research Letters*, *20*, 1479–1482. https://doi.org/10.1029/93GL01382

Zhao, Y. H., Zimmerman, M. E., & Kohlstedt, D. L. (2009). Effect of iron content on the creep behavior of olivine: 1. Anhydrous conditions. *Earth and Planetary Science Letters*, *287*(1–2), 229–240. https://doi.org/10.1016/j.epsl.2009.08.006